Journal of Organometallic Chemistry 894 (2019) 43–60

Contents lists available at ScienceDirect

Journal of Organometallic Chemistry

journal homepage: www.elsevier.com/locate/jorganchem

Crystal structure, cytotoxicity and biological activity of hydrogen bonded networks based on dimethyltin (IV) and bipodal ligands

Safaa Eldin H. Etaiw**, Dina M. Abd El-Aziz*, Elham A. Ali

Department of Chemistry, Faculty of Science, Tanta University, Tanta, Egypt

ARTICLE INFO

Article history:
Received 20 February 2019
Received in revised form
20 April 2019
Accepted 7 May 2019
Available online 13 May 2019

Keywords:
Organotin
2,2′-bipyridine
4,4′-bipyridine
1,10-Phenanthroline
X-ray structure
Antitumor activity
Antimicrobial

ABSTRACT

The supramolecular complexes (SC) of the type [Me_2SnCl_2L], L = 2,2′-bipyridine (2,2′-bpy), **SC 1**, 4,4′-bipyridine (4,4′-bpy), **SC 2,** and (1,10-phenanthroline), **SC 3,** have been synthesized and structurally characterized by elemental analysis, FT-IR, UV–Vis, ^1H and ^{13}C NMR spectra and X-ray single crystal. The X-ray data of **SC 1** and **SC 2** exhibited 1:1 stoichiometry for the dimethyltin dichloride: bipodal ligand. The structure of **SC 1** extends along the a-axis in a parallel way forming 1D-chains via H-bonds while they further propagate creating 2D-network via extensive H-bonds. The extending structure of the **SC 2** along the a-axis consists of parallel 1D-chains via H-bonds creating the A … A … A fashion. Molecular modeling studies of **SC 3** indicated that Sn(IV) center acquires N2C2Cl2 octahedral geometry. The tested compounds **SC 1**, **SC 2** and **SC 3** were found to inhibit cell proliferation and induce high percent of apoptotic towards human breast adenocarcinoma (MCF7), liver carcinoma (HEPG2), colorectal carcinoma (HCT-116), cervical carcinoma (HELA) and prostate cancer (PC3) cell lines in vitro model within short times of treatment. The anti-Oxidant and anti-hemolytic assays employ that **SC 1** exhibits moderate antioxidant activity as well as the most potent anti-hemolysis activities compared with ascorbic acid. The antimicrobial assessment has been also studied by disc diffusion method.

1. Introduction

Metal-organic polymer is a branch of modern science which is developing through the combination of polymer chemistry with supramolecular chemistry [1,2]. The supramolecular polymers are generally generated by self-assembly of complementary monomeric compounds via the formation of coordinate bonds, hydrogen bonds and π-π stacking. Constituents of the chain are linked through reversible connections enabling the polymer to grow, shorten, rearrange and adapt, this class of compounds is defined as 'dynamic combinatorial materials [2] and is currently drawing a great deal of attention [3,4]. Organotin(IV) complexes have gained relevant attention because of the ability of tin to afford stable bonds with organic carbon atoms as well as with heteroatoms. This gives rise to considerable structural diversity and topologies [5–9]. A multitude of structure types, including monomers, dimers, tetramers, oligomeric, ladders, and hexameric drums, have been discovered [10]. Also, the Lewis acid character of organotin compounds is particularly well suited for their use as building blocks in assembling coordination complexes or polymers. Organotin compounds have been known to show bioactivities, in particular as potential biocidal (e.g., antimicrobial, antifungal) [11,12]. Some also inhibit a wide variety of cancer cell lines including cell lines associated with ovarian, colon, lung, prostrate, pancreatic and breast cancer [13]. Among main group metal compounds, they appear to exhibit the most potent antitumor activities, in some cases being more effective than cis-platin in vitro tests [14,15]. Although 2,2′- and 4,4′-bipyridine and they analogues, which are neutral linear ligands, had been extensively used in transition metal chemistry [16–21] as ligands or used as excellent spacers in the construction of novel supramolecular frameworks including diverse non-covalent interactions [22–24], their use in main-group chemistry appears limited [25,26]. The first structural examples of tin complexes described the isostructural of 2:1-tri-p-tolyltin halide complexes in which the 4,4′-bpy ligand bridges two tri-p-tolyltin halide entities [27] and the structure of [$SnCl_2(CH_3)_2(C_{10}H_8N_2)$] in which 4,4′-bpy moiety bridges adjacent di-chloro dimethyl tin molecules to form a linear chain [28].

* Corresponding author.
** Corresponding author.
E-mail addresses: safaaetaiw@hotmail.com, safaaetaiw@science.tanta.edu.eg (S.E.H. Etaiw), drdinamoh@yahoo.com, dina.abdelaziz@science.tanta.edu.eg (D.M. Abd El-Aziz).

https://doi.org/10.1016/j.jorganchem.2019.05.007
0022-328X/

In this paper, we report the synthesis, crystal structure and biological activities of dimethyltin(IV) complexes of the type [Me_2SnCl_2.(L)]n, L = 2,2′-bipyridine (2,2′-bpy), **SC 1**, 4,4′-bipyridine (4,4′-bpy), **SC 2**, and 1,10-phenanthroline (1,10-phen), **SC 3**. Spectral characteristics of SC **1**–**3** were investigated with a study on the antitumor activity in vitro against various human cancer cell lines and also they were screened for their antioxidant, antihaemolytic, antibacterial and antifungal activities.

2. Experimental

2.1. Materials and methods

All reagents were purchased from Aldrich and used without further purification. Infrared spectra from 4000 to 400 cm^{-1} were recorded on a BRUCKER FT-IR instrument, using KBr pellets. Microanalyses (C, H, N) were carried out with a Perkin-Elmer 2400 automatic elemental analyzer. The mass spectra were recorded on a GCMS-Finnigan SSQ 70000. Thermogravimetric analyses were carried out on TGA–50H thermal analyzer (under N_2 atmosphere), in the range of 25–800 °C at a heating rate 20 °C/min. The electronic absorption spectra as solid matrices were measured on a Shimadzu (UV–3101PC) spectrometer and the fluorescence spectra as solid matrices were measured with a Perkin–Elmer (LS 50 B) spectrometer. ^1H and ^{13}C NMR spectra were recorded on a Bruker DPX 200 spectrometer, using DMSO-d_6 as a solvent. Structural measurements were performed on a Kappa CCD Enraf-Nonius FR590 four circle goniometer with graphite monochromatic MoKα radiation source (λ = 0.71073 A°) at 25 ± 2 °C and 20 mA/50 kV.

2.2. X-ray crystallography and structure determination

Crystal structure determinations were performed using a Kappa CCd Enraf Nonius FR 90 four circle goniometer with graphite monochromatic MoKα radiation {[λMoKα] = 0.71073 Å}. The well-developed crystals were mounted on glass fibers, and the measurements were made at 25 ± 2 °C. The structures were solved using direct-methods and all of the non-hydrogen atoms were located from the initial solution or from subsequent electron density difference maps during the initial stages of the refinement. After locating all of the non-hydrogen atoms in the structure, the model was refined against F^2, first using isotropic and finally anisotropic thermal displacement parameters. The positions of the hydrogen atoms were then calculated and refined isotropically, and a final cycle of refinements was performed. For structure visualizations, either the CERIUS2 V4.0 or Mercury 3.8 software was applied. Structure solution, refinement and data output were completed using SHELX-97 and SIR92 programs [29]. Crystal data and structure parameters for **SC 1** and **SC 2** are listed in Table 1.

Table 1
Crystal data and structure refinement parameters of SC 1 and SC 2.

	SC 1	SC 2
Empirical Formula	$C_{12}H_{14}Cl_2N_2Sn$	$C_{12}H_{14}$ Cl_2N_2Sn
Formula Weight g/mol	375.854	375.866
Temperature (K)	298	298
Crystal system	Monoclinic	Monoclinic
Space group	C 2/c	$P2_1/c$
a/Å	6.6364 (2)	6.5645(2)
b/Å	17.0155 (7)	9.9205(4)
c/Å	13.2220 (5)	10.8548(4)
α/°	90.00	90.00
β/°	104.429 (2)	95.801(2)
γ/°	90.00	90.00
V/Å3	1445.96 (9)	703.28(4)
Z	4	4
μ(Mo-Kα)/m.m-1	2.117	2.176
Calculated density/g. cm^{-3}	1.726	1.176
Goodness-of-fit on F2	0.9525	0.580
F(000)	736	368
R indices[I > 3σ(I)] R1/w*R*2	0.0427/0.0955	0.0362/0.0878
R indices(all data)	0.0699/0.1145	0.0898/0.1109
Rint	0.047	0.050
Data/restraints/parameters	1595/0/78	2574/0/79

2.3. Synthesis of the supramolecular complexes

2.3.1. Synthesis of [Me_2SnCl_2.(2,2′-bipy)], SC 1

The reaction was carried out under nitrogen atmosphere with use of standard Schlenk technique. A solution of 5-nitroisophthalic acid (0.211 g, 1.0 mmol) in mehanol was added to a solution of sodium ethoxide (0.136 g, 2.0 mmol) in methanol. The mixture was stirred for 10 min, then added to a mixture of 2,2′-bipy (0.3124 g, 2.0 mmol) and dimethyltin(IV) dichloride (0.44 g, 2 mmol) in methanol. The reaction has been continued about 12 h at 40 °C. After cooling down to the room temperature, the solution was filtered off. Already, after 3 weeks, colorless crystals started growing from the initially clear filtrate. After filtration, washing with small quantities of methanol and overnight drying, colorless crystals were obtained. Yield was 70% and m.p. was 220–225 °C. Anal. Calcd. for ($C_{12}H_{14}Cl_2N_2Sn$) MW = 375.854 g mol^{-1}: C, 38.35; H, 3.75; N, 7.45; Cl, 18.86; Sn, 31.58. Found: C, 38.41; H, 3.70; N, 7.38; Cl, 18.82; Sn, 31.53.

2.3.2. Synthesis of [Me_2SnCl_2.(4,4′-bipy)], SC 2

SC 2 was synthesized as the same procedure of **SC 1** using 4,4′-bipyridine (0.3123 g, 2 mmol) instead of 2,2′-bipyridine. After filtration, washing with small quantities of methanol and overnight drying, colorless crystals were obtained. Yield was 48% and m.p. was 220–226 °C. Chemical formula is ($C_{12}H_{14}C_{l2}N_2Sn$) and M. W. = 375.87 g mol^{-1}. Elemental Anal. Calc. C, 38. 46; H, 3.72; N, 7.38; Cl, 18.85; Sn, 31.48. Found: C, 38.35; H, 3.75; N, 7.45; Cl, 18.86; Sn, 31.58.

2.3.3. Synthesis of [Me_2SnCl_2.(1, 10-Phen)], SC 3

SC 3 was synthesized as in the same procedure of **SC 1** using 1, 10-Phenantharline (0.3604 g, 2 mmol) instead of 2,2′-bipyridine. White precipitate was formed from the initially clear filtrate. After filtration, washing with small quantities of methanol and overnight drying, white precipitate was obtained. All attempts to obtain single crystals are failed. Yield was 60% and m.p. = 265 °C. Chemical formula is (C14H14Cl2N2Sn) and M. W. = 399.89 g mol^{-1}. Elemental Anal. Calc. C, 42.25; H, 3.63; N, 7.22; Cl, 17.28; Sn, 29.60. Found: C, 42.05; H, 3.53; N, 7.01; Cl, 17.73; Sn, 29.69.

2.4. Biological activities

2.4.1. Antimicrobial activities

Disc diffusion method had been employed to determine the antimicrobial activity [30]. Freshly prepared spore suspension of different test microorganisms (0.5 mL of about 10^6 cells/mL) was mixed with 9.5 ml of melting sterile Sabouraud's dextrose medium (for fungi) or nutrient agar medium (for bacteria) at 45 °C, poured on sterile Petri dishes, and left to solidify at room temperature. Regular cellulose filter paper discs of 6 mm diameter were prepared under aseptic conditions. Each disc was saturated with 20 mg of each tested suspended material. Three replicas were made for each test, and all plates were incubated at 27 °C for 48 h for fungi, and at 32 °C for 24 h for bacteria. Then the average diameters of inhibition zones were recorded in millimeters, and compared for all plates.

2.4.2. Antioxidant screening assay (ABTS method)

For each tested compound, 2 mL of 2,2-azino-bis-(3-ethylbenzthiazoline-6-sulfonic acid) (ABTS) solution (60 μM) was added to 3 M magnesium oxide (MnO_2) solution (25 mg/mL) all prepared in 5 mL aqueous phosphate buffer solution (pH 7, 0.1 M). The mixture was shaken, centrifuged, filtered, and then the absorbance ($A_{control}$) of the resulting green-blue solution (ABTS radical solution) was adjusted at approx. 0.5 at 734 nm At that point, 50 μL of (2 mM) solution of the tested compound in spectroscopic review methanol/phosphate buffer (1:1) was included. The absorbance (A_{test}) was measured and the reduction in color intensity was expressed as % inhibition. The inhibition for each tested compound was calculated according the following equation [31–34].

$$\%\ Inhibition = \frac{A_{control} - A_{test}}{A_{control}} \times 100$$

L-Ascorbic acid (vitamin C) was utilized as standard anti-oxidant (positive control). Blank sample was run without ABTS and using methanol/phosphate buffer (1:1) instead of sample. Negative control sample was run with methanol/phosphate buffer (1:1) instead of the tested compound.

2.4.3. Antioxidant activity screening assay for erythrocyte hemolysis

The blood was obtained from rats by cardiac puncture and gathered in heparinized tubes. Erythrocytes were isolated from plasma and the buffy coat was washed three times with 10 vol of 0.15 M NaCl. Amid the last wash, the erythrocytes were centrifuged at 2500 r/min for 10 min to acquire a constantly packed cell preparation. Erythrocyte hemolysis was intervened by peroxyl radicals in this measure coordination polymer system [35]. A 10% suspension of erythrocytes in phosphate buffered saline pH 7.4 (PBS) was added to the same volume of 200 mM AAPH solution in PBS containing samples to be tested at different concentrations. The reaction mixture was shaken delicately while being brooded at 37 °C for 2 h. The reaction mixture was then evacuated, diluted with eight volumes of PBS and centrifuged at 1500 g for 10 min. The absorbance of the supernatant was read at 540 nm [35]. Also, the reaction mixture was treated with 8 vol of distilled water to achieve complete hemolysis, and the absorbance of the supernatant obtained after centrifugation was measured at 540 nm. L-ascorbic acid was utilized as a positive control.

2.4.4. Antitumor activity

In vitro potential cytotoxicity of the tested compound was performed using the colorimetric method [36]. The tested compounds dissolved in dimethylsulfoxide (DMSO) were subjected to cytotoxic evaluation against human breast adenocarcinoma cell line (MCF7), liver carcinoma (HEPG2), colorectal carcinoma (HCT-116), cervical carcinoma (HELA) and prostate cancer (PC3) cell lines. Human lung fibro blast cell line (WI -38) was used as a normal cell line for comparison of the effect of the tested **SC 1**–**3** on the five tumor cell lines. 5-fluorouracil was utilized as a standard anticancer drug for comparison. The cell lines were obtained from ATCC via Holding company for biological products and vaccines (VACSERA), Cairo, Egypt. This colorimetric assay is based on the conversion of the yellow 3-(4,5-dimethylthiazol-2-yl)-2,5-diphenyltetrazolium bromide (MTT) to a purple formazan derivative by mitochondrial succinate dehydrogenase in viable cells. The cells were cultured in RPMI-1640 medium with 10% fetal bovine serum. Antibiotics added were 100 units/ml penicillin and 100μg/ml streptomycin at 37 °C in a 5% CO_2 incubator. The cells were seeds in a 96-well plate at a density of 1.0 × 104 cells/well at 37 °C for 48 h under 5% CO_2 [37]. After incubation the cells were treated with different concentrations of the tested compound and incubated for 24 h. After 24 h of drug treatment, 20 μl of MTT solution at 5 mg/ml was added and incubated for 4 h. Dimethyl sulfoxide (DMSO) in volume of 100 μl is added into each well to dissolve the purple formazan formed. The colorimetric assay is measured and recorded at absorbance of 570 nm using a plate reader (EXL 800, USA). The relative cell viability in percentage was calculated as (A570 of

Table 2
Bond lengths (Å) and bond angles (deg.) of SC 1.

Sn1– N3	2.400(3)	Cl2–Sn1–Cl2	104.84(6)
Sn1– Cl2	2.5348(12)	N3–Sn1–C9	90.53(15)
Sn1– C9	2.124(4)	Cl2–Sn1–N3	69.03(19)
Sn1– Cl2	2.5348(12)	C9–Sn1–N3	93.07(10)
Sn1– N3	2.400(3)	Cl2–Sn1–N3	88.64(18)
Sn1– C9	2.124(4)	N3–Sn1–N3	162.10(10)
N3– C4	1.333(6)	C9–Sn1–Cl2	88.64(18)
N3– C8	1.355(5)	C9–Sn1–C9	90.53(15)
C4– C5	1.380(7)	Cl2–Sn1–C9	175.5(3)
N3–Sn1–Cl2	162.10(10)	Cl2–Sn1–C9	92.21(16)
N3–Sn1–C9	87.66(19)	N3–Sn1–C9	87.66(19)
Cl2–Sn1–C9	92.21(16)	Sn1–N3–C4	122.0(3)
N3–Sn1–Cl2	93.07(10)	Sn1–N3–C8	118.1(3)

Table 3
Bond lengths (Å) and bond angles (deg.) of SC 2.

Sn1–C8^{i}	2.121 (4)	C8^{i}–Sn1–C8	180.0
Sn1–C8	2.121 (4)	C8^{i}–Sn1–N3	91.10 (16)
Sn1–N3	2.412 (3)	C8–Sn1–N3	88.90 (16)
Sn1–N3^{i}	2.412 (3)	C8^{i}–Sn1–N3^{i}	88.90 (16)
Sn1–Cl2	2.5741 (10)	C8–Sn1–N3^{i}	91.10 (16)
Sn1–Cl2^{i}	2.5741 (10)	N3–Sn1–N3^{i}	180.0
N3–C7	1.316 (5)	C8^{i}–Sn1–Cl2	89.71 (13)
N3–C6	1.321 (5)	C8–Sn1–Cl2	90.29 (13)
C4–C9	1.358 (5)	N3–Sn1–Cl2	90.58 (8)
C4–C5	1.384 (5)	N3^{i}–Sn1–Cl2	89.42 (8)
C4–C4^{iii}	1.487 (7)	C8^{i}–Sn1–Cl2^{i}	90.29 (13)
C5–C7	1.381 (5)	C8–Sn1–Cl2^{i}	89.71 (13)
C7–N3–C6	116.6 (3)	N3–Sn1–Cl2^{i}	89.42 (8)
C7–N3–Sn1	121.5 (2)	N3^{i}–Sn1–Cl2^{i}	90.58 (8)
C6–N3–Sn1	121.7 (3)		

Symmetry codes: (i) -x, 1/2 + y, 1/2-z; (ii) 1-x, 3/2 + y, 1/2-z.

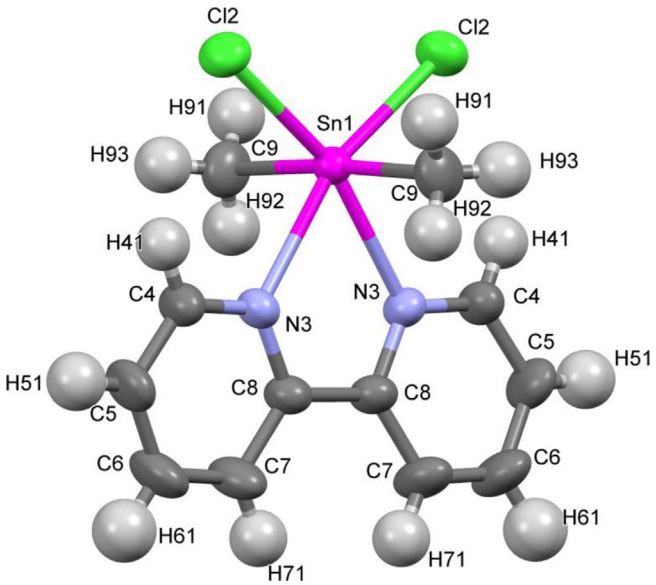

Fig. 1. Asymmetric unit of SC **1** showing the atom labeling scheme and thermal ellipsoids are shown 50% probability.

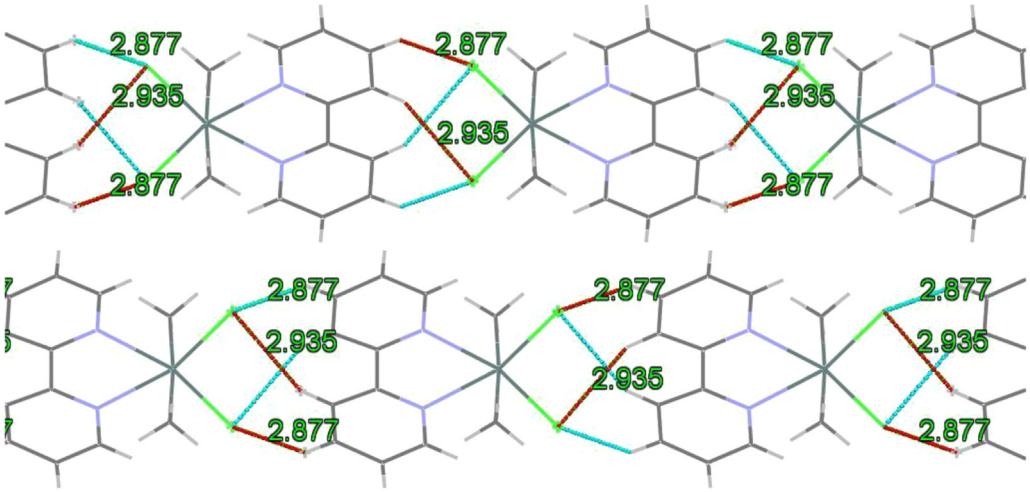

Fig. 2. View of the network structure of SC **1**, showing the 1D-chains along the a-axis via H-bonds.

treated samples/A570 of untreated sample) X 100. The relation between surviving fraction and drug concentration is plotted to get the survival curve of each tumor cell line. The 50% inhibition concentration (IC_{50}) was determined by curve fitting.

3. Results and discussion

3.1. X-ray crystal structures of [Me_2SnCl_2.(2,2′-bipy)], SC 1 and [Me_2SnCl_2.(4,4′-bipy)], SC 2

The reactions of the ternary adducts dimethyltin(IV) dichloride and 5-nitroisophthallic acid (NIP) in the presence of sodium ethoxide and 2,2′-bipyridine (2,2′-bipy) or 4,4′-bipyridine (4,4′-bipy) in methanol under nitrogen atmosphere at 40 °C afford colorless cubic crystals of the mono nuclear and mono-ligand adduct of the empirical composition [Me_2SnCl_2.(2,2′-bpy)], **SC 1** and [Me_2SnCl_2.(4,4′-bipy)], **SC 2,** respectively, which are NIP free**.** Many trials had been carried out to coordinate 5-nitroisophthallic acid to the tin atom which ended up so far unsuccessfully. The **1** and **2** are diamagnetic and sufficiently stable against air-oxidation when well dried. They are insoluble in many common non-polar and polar solvents while they are soluble in DMF and DMSO. The lattice constants, density and refinement parameters of **SC 1** and **SC 2** are collected in Table 1, while the intermolecular bond lengths

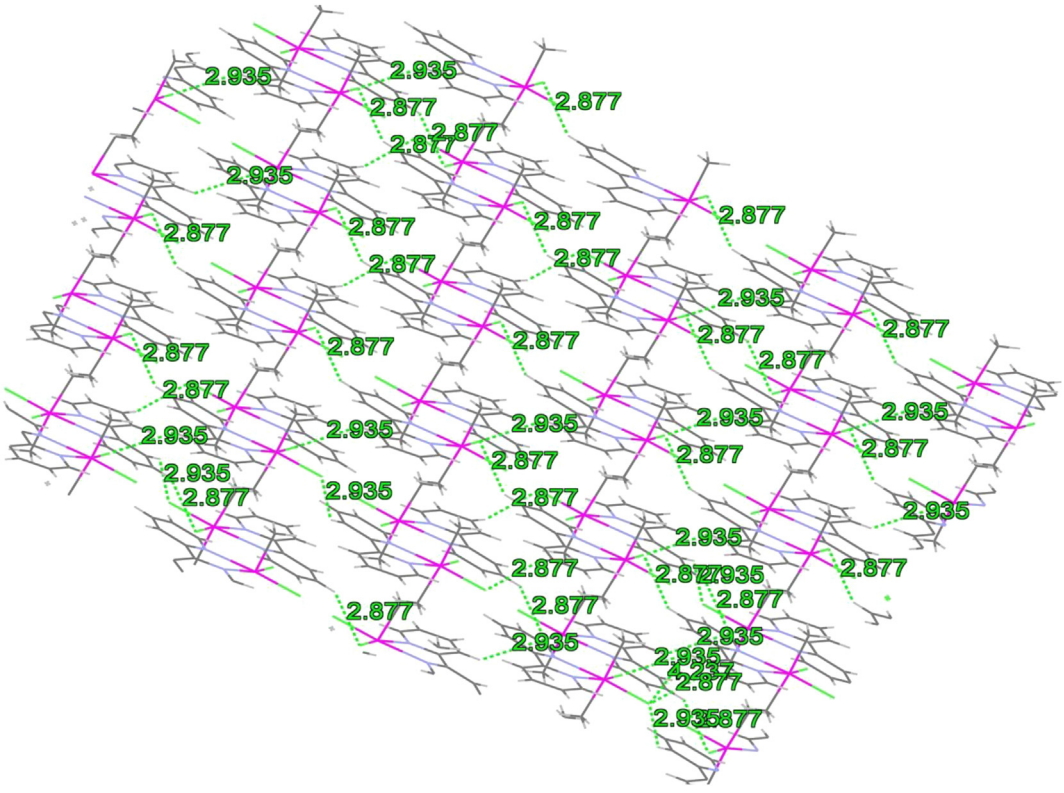

Fig. 3. Perspective view of the 2D-structure of SC 1 via H-bonds along the ab-plane.

and bond angles are collected in Tables 2 and 3. The cell units of **1** and **2** confirm the assignment of 1:1 stoichiometry for the dimethyltin dichloride: bipyridine ligand which exhibit Z = 4 and atom size occupancy 1. The **SC 1** and **SC 2** crystallize in the monoclinic space group C 2/c and $P2_1/c$, respectively, Table 1. The asymmetric unit cell of **SC 1** contains, simply, one dimethyltin dichloride and one 2,2′-bipyridine molecules, Fig. 1. The Sn atom has an identity symmetry operation with the symmetry transformation X, Y, Z while the Cl(2) atom has inversion center symmetry operation with inversion at [0,0,0]. The tin center displays distorted octahedral coordination geometry formed by coordination of the two nitrogen atoms of the 2,2′-bpy and two Cl atoms in equatorial plane in addition to two methyl ligands in axial positions. The Sn–N bond lengths [2.40 Å] are apparently longer than the Sn–C bond lengths [2.124 Å] while the Sn–Cl bond lengths are much longer [2.535 Å]. The axial C9–Sn1–N3 and C9–Sn1–Cl2 angles are 87.64 and 90.53°, respectively and the four donor atoms on the equatorial plane are perfectly planar. The smallest equatorial bond angle is observed for N(3)–Sn(1)–N(3) (69.03°) while the other equatorial bond angles equal to 93.7° and 104.84°. The two pyridyl rings are not planar exhibiting a dihedral angle of 12.87°. The structure of **1** extends along the a-axis in a parallel way forming 1D-chains via H-bonds, Fig. 2. The Sn–Sn distance in the chain is 9.132 Å while the Sn–Sn distance between two chains is 6.636 Å. On the other hand, the structure propagates along the c-axis or in the ab-plane creating parallel rows which are connected by H-bonds (2.690–2.961 Å) forming 2D-network, Figs. 3 and 4, Table 4. The hydrogen bonds represent the only supramolecular interaction in the structure of **1**. On the other hand, the asymmetric unit of **SC 2** is composed of half molecule of each Me_2SnCl_2 and 4,4′-bipy, Fig. 5, while the extended structure contains two repeat asymmetric units, Fig. 6. The tin atom, Sn1, has an identity symmetry operation and assumes distorted octahedral structure coordinated by two N-bonded from two 4,4′-bipy and two methyl groups in equatorial

Table 4
Hydrogen bond lengths (Å) and bond angles (deg.) of SC 1.

D-H … A	d(D-H)	d(H … A)	d(D … A)	∧(DHA)
C7–H7^{i} … … Cl2	0.960	2.791(2)	3.492	130.76
C11–H11 …. .Cl2	0.960	2.995(3)	3.623	124.27
C13–H13^{ii} …. Cl2	0.960	2.981(2)	3.728	135.67
C5–H5 … … … Cl3	0.960	2.690(3)	3.439	135.16
C11–H11^{iii} …. .Cl3	0.960	2.953(15)	3.648	130.23
C15–H15^{ii} …. . Cl3	0.960	2.844(2)	3.635	140.31
C8–H8^{iv} … … … Cl3	0.960	2.769(2)	3.632	150.38
C17–H17A …. .N4	0.960	2.774(7)	3.052	97.48
C6–H6A … …..N4	0.960	2.826(5)	3.139	100.19
C17–H17B …. .N10	0.960	2.936(7)	3.174	95.26
C6–H6C … …..N10	0.960	2.961(7)	3.247	98.61
C17–H17A …. .C11	0.960	2.842(10)	3.607	137.21

Symmetry codes: (i) x-1,-y,z-1/2; (ii) 1/2 + x,1/2 + y,z; (iii) 1 + x,-y,1/2 + z; (iv) x-1/2,1/2 + y,z.

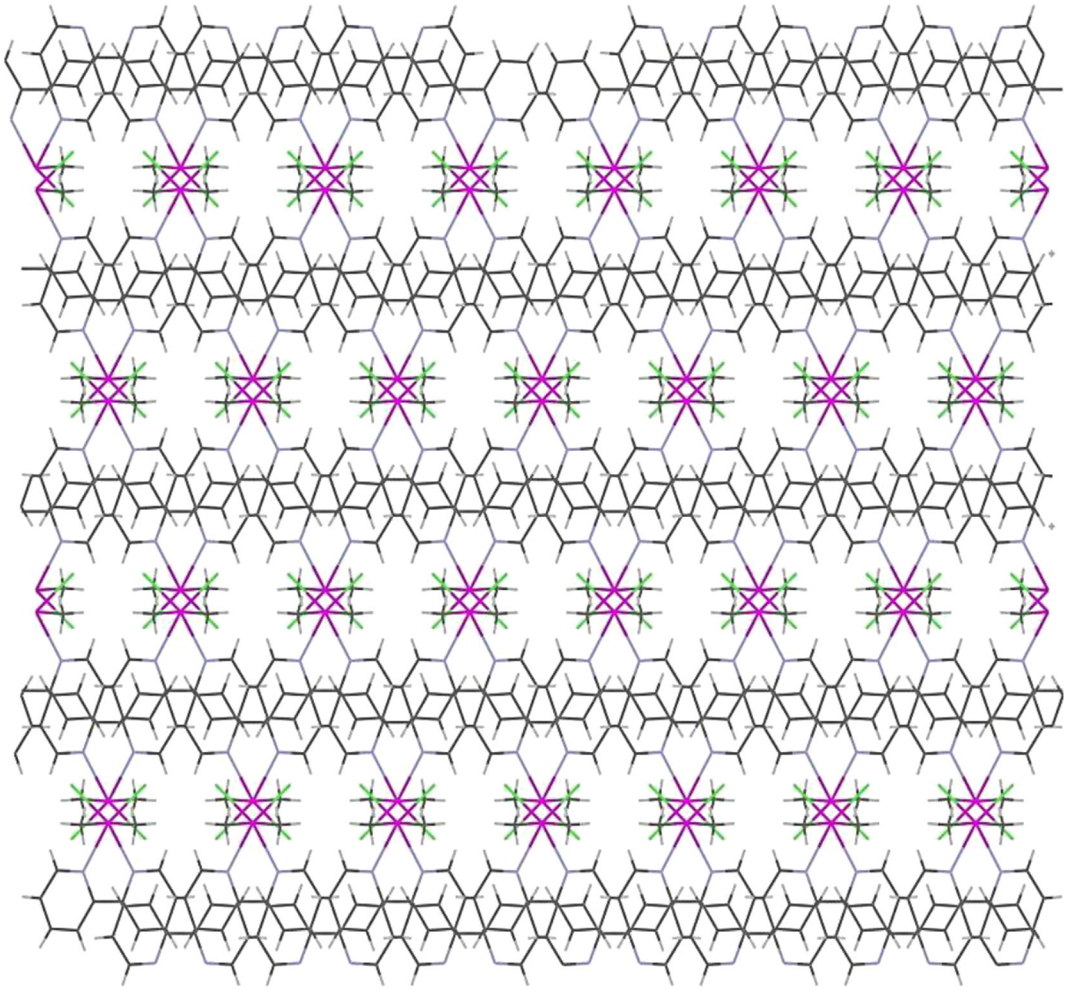

Fig. 4. View of the 2D-network structure of SC 1 down the projection of the c-axis.

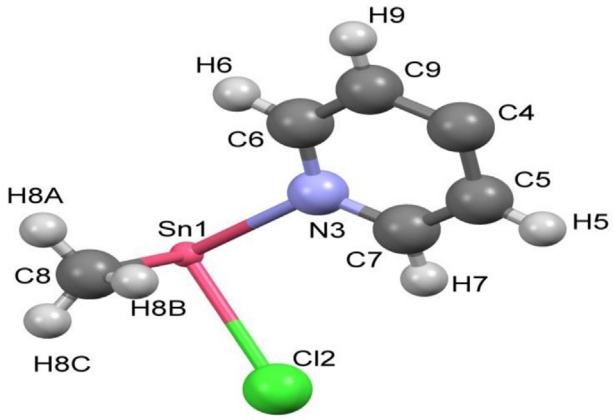

Fig. 5. The asymmetric unit of [Me_2SnCl_2.(4,4′-bipy)], SC 2.

plane as well as two Cl atoms in axial positions while all of them are trans-oriented. The Cl2 atom locates at an inversion center with inversion transformation at [0,0,0]. The extending structure of the **2** along the a-axis consists of parallel 1D-chains exhibiting A … A … A fashion. The separation distance between the successive chains along b-axis is Sn1 …. Sn1 = 7.353 Å. These chains are connected by hydrogen bonds (2.817–3.062 Å) forming 2D-layer, Fig. 7. The SnN2C2Cl2 octahedral are slightly distorted with distances in the range of 2.121(4) Å to 2.5741(10) Å and angles between 88.90(16)°, 91.10(16)° and 180°, Fig. 7 and Table 3. The $C8^{i}$-Sn1-C8 and N3–Sn1–$N3^{i}$ fragments are almost linear with angle being 180°, Table 3. The bond lengths and bond angles are in the range of the prototype complexes [9,38]. Detailed structural analyses revealed that the one dimensional chains are bonded to another chains by hydrogen bonds between the chloride atoms of Me_2SnCl_2 molecule in one chain and the hydrogen atoms of 4,4\-bpy ligands in another chain, organizing these chains into a two dimensional layer Table 5, Fig. 7. The extending structure of the 3D-network structure of **SC 2** along c-axis exhibits the methyl groups located in the space of the boxes which formed by crossing the chains of **2**, Fig. 8. Furthermore,

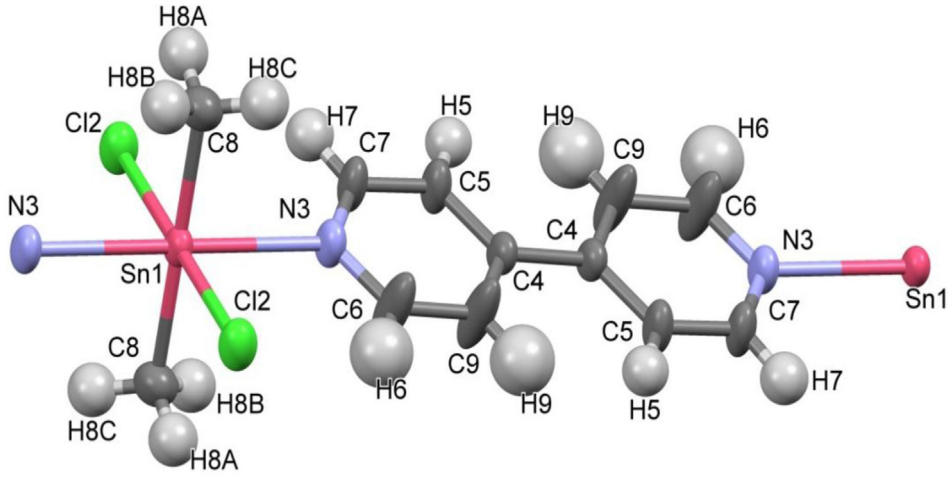

Fig. 6. An ORTEP plot contains two repeat asymmetric units of the SC 2 [Me_2SnCl_2.(4,4′-bipy)], with atom labeling scheme and thermal ellipsoids are shown 50% probability.

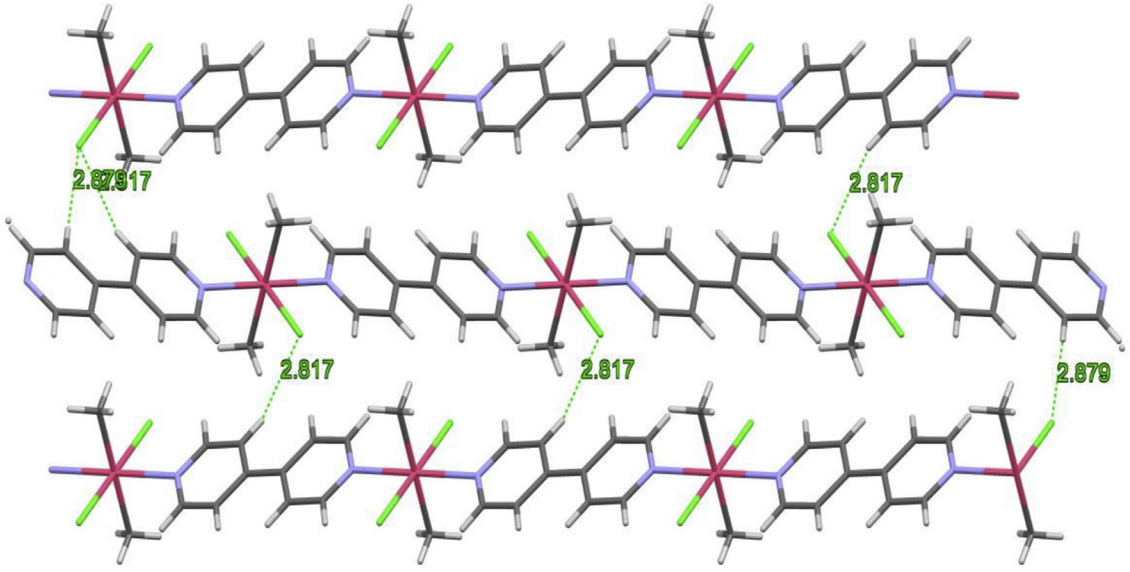

Fig. 7. View of the 1D-chains of the SC 2 down the projection of a-axis showing the parallel chains connected by H-bonds forming 2D-layer.

Table 5
Hydrogen bond lengths (Å) and bond angles (deg.) of the SC 2.

D-H …. A	d(D-H)	d(H …. A)	d(D …. A)	∧(DHA)
C14–H14 … …N8	0.961	2.657	3.327	127.15
C10–H10 … …N8 iii	0.960	2.577	3.264	128.68
C14–H14 … …O9	0.961	2.434	2.753	99.01
C7–H7 … …..O17	0.960	2.553	2.834	96.95
C10–H10 … …17v	0.960	2.463	3.154	128.69
C12–H122 … …O17	0.960	2.588	2.644	82.73
C12–H121 … …O17	0.960	2.632	2.644	80.24
C12–H122 …. …C7	0.960	2.890	3.642	136.00

Symmetry codes: 1-x, 3/2 + y, 1/2-z.

these chains spread in three dimensions crossing each other feathering three-dimensional network through hydrogen bonds, Table 5, and edge to face π … π interactions between centroid (N3C6C9C4C5C7) and H7 with a distance equals to 3.861 Å and centroid (N3C7C5C4C9C6) and H7 with a distance equals to 3.3081 Å, Fig. 9. These supramolecular forces cause effective backing of the network structure of the **SC 2**.

3.2. Molecular modeling of [Me_2SnCl_2.(1, 10-Phen)], SC 3

The geometry of **SC 3** was optimized using DMOL3 program [39] in Materials Studio package, which is designed for the realization of large scale density functional theory (DFT) calculations. DFT semi-core pseudopods calculations (dspp) were performed with the double numerica basis sets plus polarization functional (DNP). The DNP basis sets are of comparable quality to 6-31G Gaussian basis sets [40]. Delley et al. showed that the DNP basis sets are more accurate than Gaussian basis sets of the same size. The RPBE functional [41] is so far the best exchange–correlation functional [42], based on the generalized gradient approximation (GGA), which is employed to take account of the exchange and correlation effects of electrons. The geometric optimization is performed without any symmetry restriction. Geometric and electronic structure of **SC 3** was calculated by the optimization of its bond lengths and bond angles, Table 6. Molecular modeling studies were performed to get a preferable perception for geometrical structure of the investigated compound. The Sn(IV) center in **SC 3** acquires $N_2C_2Cl_2$ octahedral geometry. The bond distances N(14)–Sn(15) and N(9)–Sn(15) are 2.761 and 2.756 Å, respectively. The bond distances of Sn with two axial chloride atoms, Sn(15)–Cl(17) and Sn(15)–Cl(16), are 3.04 and 2.998 Å, respectively. In addition, the bond angles, Cl(17)-Sn(15)-N(14) 93.539, Cl(17)-Sn(15)-N(9) 89.139, Cl(17)-Sn(15)-Cl(16) 176.128, N(14)-Sn(15)-N(9) 61.159 indicate that the coordination environment around the Sn is slightly distorted octahedral geometry. The theoretical Molecular Electrostatic Potential (MEP) was mapped onto electron density isosurface. Therefore, the electrostatic potential values are laid on three dimensionally (3D-) molecular modeling that predict the approximate size and shape of the molecule. Electrostatic potential maps present information about the charge distribution of the molecule because of the properties of the nucleus and the nature of electrostatic potential energy. Given that the radial value of the isosurface is dependent on the electron density, larger molecules with more electrons will have larger isosurface values than smaller molecules with fewer electrons. The radial value of the isosurface is the radius value that will be used in the electrostatic potential energy equations. The electrostatic potential values (ESP), Energy components: Sum of atomic energies = −1689.1600212Ha, Kinetic = −7.5172892Ha, Electrostatic = −2.3497623Ha, Exchange-correlation = 2.1237292Ha, Spin polarization = 1.6720276Ha, Total Energy = −1695.231316Ha, Binding energy = −6.0712947Ha. The

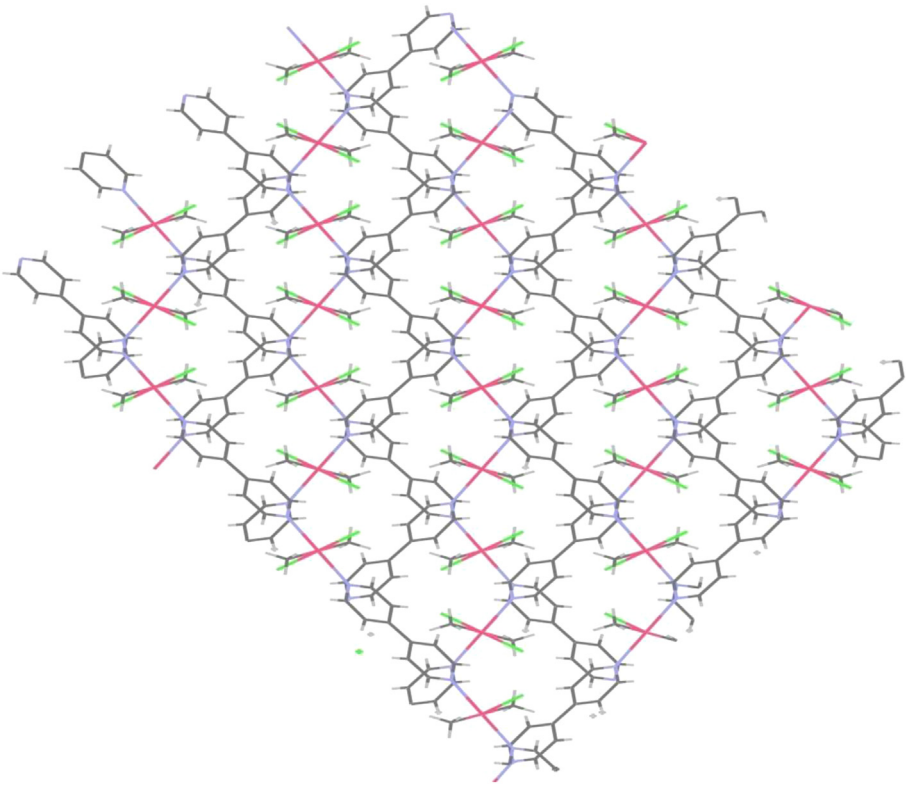

Fig. 8. Visualization of the 3D-network structure of the SC 2 down the projection of c-axis showing the methyl groups located in the space of the boxes formed by crossing the chains of the complex.

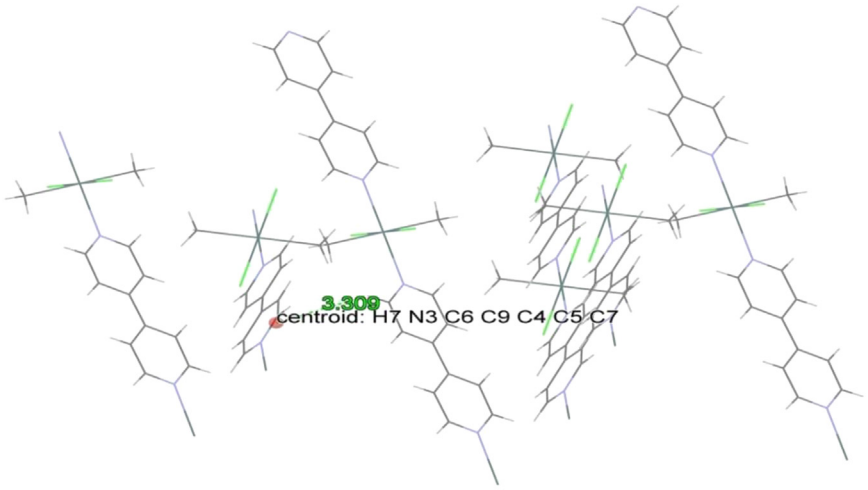

(a)

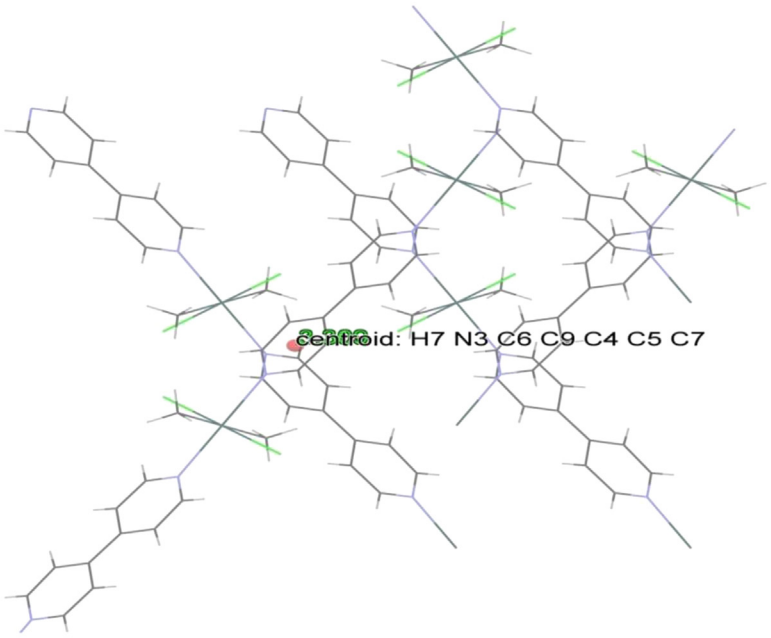

(b)

Fig. 9. Edge to face π …. π stacking supramolecular forces causing backing of the network structure of SC 2.

optimized molecular structure of the **SC 3** with minimum energy obtained from the calculations and 3D-Molecular electrostatic potential isosurface were shown in Fig. 10. The photo-induced charger distribution over the whole molecular skeleton of **3** is represented by plot of the Frontier molecular orbitals (HOMO and LUMO) as given in Fig. 11. E_{HOMO} is a quantum chemical descriptor which is often associated with the electron donating ability of the molecule. High value of E_{HOMO} likely indicates a tendency of the molecule to donate electrons to appropriate acceptor molecule of low empty molecular orbital energy. Therefore, E_{LUMO} indicates the ability of the molecule to accept electrons. It is well known that lower value of E_{LUMO}, the more probable for the molecule to accept electrons [43]. The HOMO electronic density distribution for **3** can be represented as localization of charge density on the nitrogen atoms and dienes of 1,10-phenathroline moiety. The HOMO electronic density distribution for **3**, at −5.939 eV. In the case of LUMO level, the charge is mostly localized that can facilitate the back donation from Sn to nitrogen atoms of 1,10-phenathroline moiety. The LUMO level lies at −3.709 eV. Quantum chemical parameters, (E_{HOMO}), (E_{LUMO}) and the energy gap ($E = E_{LUMO} - E_{HOMO}$), are found to be −5.939, −3.709 and 2.23 eV, respectively.

Table 6
Molecular modeling data of [Phen.Me_2SnCl_2], SC 3.

Bond length		Bond angle	
Sn(15)–C(19)	2.444	C(19)-Sn(15)-C(18)	97.459
Sn(15)–C(18)	2.449	C(19)-Sn(15)-Cl(17)	89.137
Sn(15)–Cl(17)	3.04	C(19)-Sn(15)-Cl(16)	87.321
Sn(15)–Cl(16)	2.998	C(19)-Sn(15)-N(14)	105.246
N(14)–Sn(15)	2.761	C(19)-Sn(15)-N(9)	166.149
N(9)–Sn(15)	2.756	C(18)-Sn(15)-Cl(17)	90.847
N(9)–C(10)	1.372	C(18)-Sn(15)-Cl(16)	88.065
C(8)–H(24)	1.096	C(18)-Sn(15)-N(14)	156.922
C(8)–N(9)	1.359	C(18)-Sn(15)-N(9)	96.308
C(7)–H(23)	1.095	Cl(17)-Sn(15)-Cl(16)	176.128
C(7)–C(8)	1.421	Cl(17)-Sn(15)-N(14)	93.539
C(6)–H(22)	1.098	Cl(17)-Sn(15)-N(9)	89.139
C(6)–C(7)	1.417	Cl(16)-Sn(15)-N(14)	88.903
		Cl(16)-Sn(15)-N(9)	94.672
		N(14)-Sn(15)-N(9)	61.159

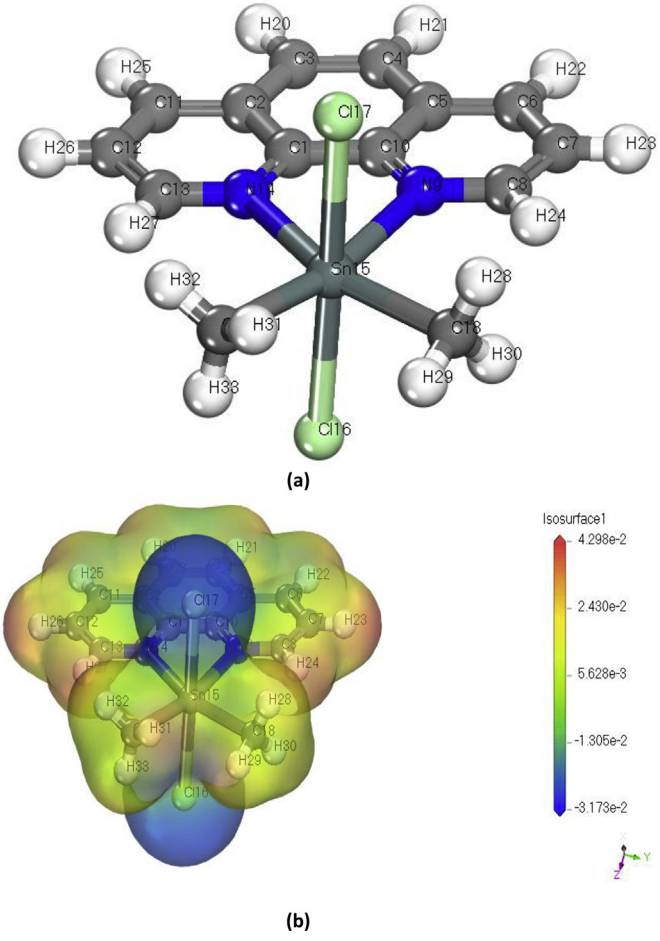

Fig. 10. Optimized geometry of SC 3 (a) and 3D-Molecular electrostatic potential isosurface (b).

3.3. IR and NMR spectra of SC 1, SC 2 and SC 3

The presence of the aromatic systems in the structures of **SC 1, SC 2 and SC 3** was confirmed by their IR spectra which display the stretching frequencies of interest, Table 7 and Figs. S1–S3. The $\nu_{(C=C)}$ and $\nu_{(C=N)}$ bands exhibit slightly shift than that of the free ligand supporting the coordination of ligand to the Sn(IV) atom. The medium bands at 2915-2854 cm^{-1} correspond to $\nu_{CH(aliphatic)}$ of the methyl groups, supporting the presence of the dimethyltin units.

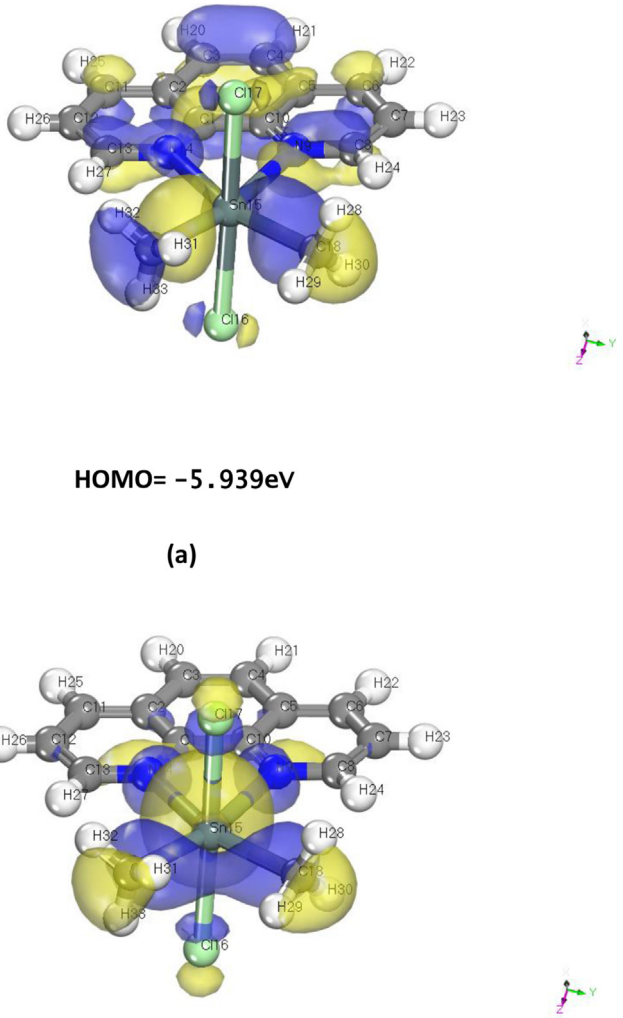

Fig. 11. HOMO (a) and LUMO (b) representation of SC 3.

Table 7
IR spectra of SC 1-3.

No.	Compound	$\nu_{(CH)}$ (arom)	$\nu_{(CH)}$ (aliph)	$\nu_{(C=N)}$ and $\nu_{(C=C)}$ (arom.)	δ_{CH} of L	γ_{CH} of L	$\nu_{(Sn-C)}$	$\nu_{(Sn-N)}$
SC 1	[Me_2SnCl_2.(2,2′-bipy)]	3104, 3054, 3028	2915, 2880	1597, 1491	1317	767, 648	573	465
SC 2	[Me_2SnCl_2.(4,4′-bipy)]	3090, 3065, 3010	2917, 2854	1534, 1491	1332	727, 627	572	481
SC 3	[Me_2SnCl_2.(1, 10-Phen)]	3058, 3008	2916, 2850	1585, 1455	1348	725, 683	577	420

Also, the IR spectra show the stretching vibrations of Sn–C bond that appears as a medium band in the region of 572–577 cm^{-1}. On the other hand, the stretching vibrations of Sn–N bond appear in the region of 465–481 cm^{-1}, confirming the coordination of nitrogen atoms of the bipodal ligands to Sn atom. The ^{1}H- and ^{13}C NMR spectra of the **SC 1, SC 2 and SC 3** show their expected integration and signal multiplicities as complexes containing the Me_2SnCl_2 and organic bipodal ligands, Table 8 and Figs, S4-9. ^{1}H NMR spectra of the **SC 1**–**3** display distinct signals corresponding to the 2,2′-bpy, 4,4′-bpy and 1, 10-Phen ligands which suffer shifts to down field than those of the ligands due to coordination to tin atom and formation of H- bonds, Table 8. Also, the spectra of **1**–**3** show a well-defined singlet at 1.03, 1.05 and 0.938 ppm, respectively, attributed to the methyl protons attached to the tin atom. These singlet signals are accompanied by two Sn(IV) satellites at 0.083 and 1.26 ppm, $^2J_{(1H-119Sn)}$ coupling constant = 46.0 Hz for SC **1**, at 0.083 and 1.26 ppm, $^2J_{(1H-119Sn)}$ coupling constant = 46.0 Hz for SC **2** and at 0.764 and 1.126 ppm, $^2J_{(1H-119Sn)}$ coupling constant = 46.0 Hz for SC **3**, which fall in the range for six-coordinate dimethyltin(IV) species forming octahedral coordination geometry. The singlet band at 3.42 ppm is due to the protons of the water molecules. On the other hand, ^{13}C-spectra of **SC 1**–**3** exhibit characteristic signals for the bipodal ligands; at 121.29–150.48 ppm which appear at more or less the same positions of those of the ligands, Table 8. The Me_2Sn units give rise to a peak at 22.0, 22.63 and 22.8 ppm for **1**–**3**, respectively. The singlet signals of **SC2** and **3** are accompanied by two characteristic satellites due to spin coupling with $^{119/117}$Sn nuclei while the spectrum of **SC1** exhibits weak ill-defined satellites. The values of ^{1}J ($^{119/117}$Sn–^{13}C) for **SC2** and **3** 860 and 800 Hz, respectively, indicating that tin atoms in these complexes are six-coordinate in solution exhibiting octahedral geometry with two methyl ligands in axial positions. Thus, the IR and NMR spectra confirm the presence of the organic ligand as well as the Me_2Sn units. Consulting the IR data (as solid state) and NMR spectroscopic data (in solution) of **SC 1**–**3**, indicates that the structural features of these complexes in the solid state are consistent with those in solution. (NMR studies). In addition, the coupling constant values of ^{1}H- and ^{13}C- tin NMR signal support the octahedral coordination geometry of tin present in the structure of these complexes. The ratio between the signals area of all compounds in the ^{1}H NMR spectra support the composition elucidated by X-ray diffraction and elemental analysis.

3.4. Electronic absorption and emission spectra

The UV/Vis absorption spectrum of **SC 1** reveals three absorption bands at 225, 260 and 340 nm, Fig. S10. The first two high energy bands are due to $^1L_a \leftarrow {}^1A$ and $^1L_b \leftarrow {}^1A$ transitions, respectively. These bands are shifted to lower wavelengths than those of 2,2′-bipy (232 nm, $^1L_a \leftarrow {}^1A$ and 278 nm, $^1L_b \leftarrow {}^1A$) [44], confirming the coordination of the nitrogen atoms of the ligand to the tin atom**.** The third band at 340 nm is due to $\pi-\pi^*$ transitions. The weak absorption band of the 2,2′-bpy ligand at 390 nm corresponding to $n-\pi^*$ transitions disappears in the spectrum of **SC 1** supporting participation of the nitrogen atoms of 2,2′-bpy in the coordination sphere of tin. The UV/Vis absorption spectrum of the **SC 2,** Fig. S11, displays the absorption bands of 4,4′-bipy ligand in addition to the CT bands. The absorption bands of the 4,4′- bipyridine ligand

Table 8
1H and ^{13}C NMR spectral data of the bipodal ligands and SC 1-3.

Compound	^{1}H δ_{ppm}	Assignment	^{13}C δ_{ppm}	Assignment
2,2′-bipy	7.12	$H_{4,4'}$	149.30	$C_{3,3'}$
	7.66	$H_{5,5'}$	120.80	$C_{4,4'}$
	8.50	$H_{6,6'}$	137.20	$C_{5,5'}$
	8.59	$H_{3,3'}$	124.20	$C_{6,6'}$
[Me_2SnCl_2.(2,2′-bipy)]	7.42–7.45	2,2′-bipy	149.17	2,2′-bipy
	7.86–7.97		120.40	
	8.41–8.43		137.31	
	8.71–8.73		124.27	
	1.03	Me	21	
	0.08, 1.26	Sn(IV) satellites		Me
4,4′-bipy	7.60	$H_{2,2'}$ and $H_{6,6'}$	149.90	$C_{2,2'}$ and $C_{6,6'}$
	8.56	$H_{3,3'}$ and $H_{5,5'}$	144.50	$C_{4,4'}$
			121.30	$C_{3,3'}$ and $C_{5,5'}$
[Me_2SnCl_2.(4,4′-bipy)]	7.77–7.80	4,4′-bipy	150.48	4,4′-bipy
	8.70–8.72		144.35	
	1.05–1.06	Me	121.29	
	0.08, 1.24	Sn(IV) satellites	22.63	Me
1, 10-Phen	7.26	$H_{2,7}$	121.50	$C_{2,7}$
	7.55	$H_{4,5}$	127.60	$C_{4,5}$
	8.00	$H_{3,6}$	136.40	$C_{3,6}$
	8.81	$H_{1,8}$	150.00	$C_{1,8}$
[Me_2SnCl_2.(1, 10-Phen)]	8.06–7.10	1, 10-Phen	124.89	1, 10-Phen
	8.195		126.79–129.29	
	8.80–8.87		139.01	
	9.46–9.48		148.674	
	0.938	Me	22	Me
	0.76, 1.13	Sn(IV) satellites		

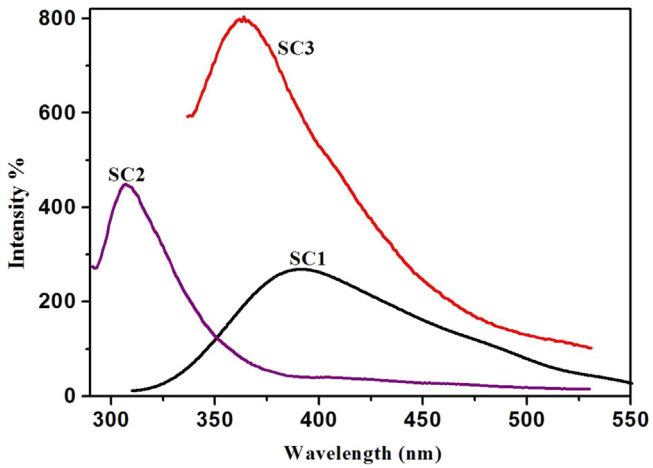

Fig. 12. Emission spectra of SC 1–3 in solid state.

reveals three absorption bands at (218 nm, $^1L_a \leftarrow {}^1A$), (278 nm, $^1L_b \leftarrow {}^1A$) and (390 nm, n– π*) transitions [44]. The two high energy bands are shifted to lower wavelengths in the absorption spectrum of **SC 2**, (212 nm, $^1L_a \leftarrow {}^1A$), (255 nm, $^1L_b \leftarrow {}^1A$), confirming the complex formation. The weak absorption band of the 4,4′-bipyridine ligand at 390 nm corresponding to n– π* transitions disappears in the spectrum of **SC 2** supporting participation of the nitrogen atoms of 4,4′- bpy in the coordination sphere of tin. The UV/Vis absorption spectrum of **SC 3**, Fig. S12, displays the same bands of 1,10-phenathroline at more or less the same positions except the n-π* band, which disappears supporting participation of the nitrogen atoms of 1,10-phenathroline in the coordination sphere of tin. Free 1,10-phenathroline reveals four absorption bands at 200, 225, 260 and 285 nm [44]. The first two bands are due to $^1B_a \leftarrow {}^1A$ and $^1B_b \leftarrow {}^1A$ transitions, respectively. The third band at 260 nm can be considered as a composite one. This broad band can be assigned to $^1L_a \leftarrow {}^1A$ and $^1L_b \leftarrow {}^1A$ transitions. The last long wavelength band at 285 nm is weak and corresponds to n–π* transition which disappears on the addition of HCl. The emission spectra of **SC 1 and SC 2** in solid state display bands at 400 and 308 nm, respectively, Fig. 12. It is worth mentioning that the emission spectrum of 2,2′-bpy and 4,4′-bip do not show any bands in solid state on excitation at 290 nm. This finding is expected as the fact that the pyridine and its derivatives are, generally, not luminescent materials [45]. On the other hand, the emission spectrum of **SC 1** reveals one band at 400 nm upon excitation at 300 nm which corresponds to the lowest π–π* state in the ligand under the effect of coordination [44]. The emission spectrum of **SC 3** in solid state displays one broad band in the region of 360–375 nm which can be considered as a composite one and a broad band at 420 nm, Fig. 12. The first band was observed in the emission spectrum of 1,10-phenathroline. It was noticed that the emission spectrum of 1,10-phenathroline displays well developed peak at 365 nm and two shoulders at 380 and 425 nm [46]. The three structured bands correspond to the close laying π–π* transitions. On the other hand, the band at 420 nm in the emission spectrum of **SC 3** corresponds to MLCT transitions.

3.5. Thermogravimetric analysis

The TGA curves of **SC 1–3** indicate that the framework of the organotin complexes can be coherent up to 125–200 °C. The degradation profile occurs in three steps starting from 150 °C up to 485 °C, Fig. S13 and Table 9. For **SC1**, the first step in the temperature range 150–200 °C corresponds to the loss of the more volatile connecting unit MeSn and 2,2′-bipyridine, Δm % obser. (calcd): 78.0 (77.18). This step is followed by the gradual release of two units of HCl in the temperature ranges 200–400 and 400–485 °C, Δm % obser. (calcd): 9.2 (9.7), 9.3 (9.7), respectively. The weight of the residue obtained after complete degradation is consistent with carbon Δm % obser. (calcd): 3.5 (3.7). The thermogram of **SC 2**, Fig. S14, indicates that the framework of the organotin complex can

Table 9
Thermal gravimetric analysis data of SC 1-3.

No	Temp. range (^{0}C)	Mass loss (%)		Assignment
		Calc.%	Found%	
SC 1	27–160	–	–	Thermally stable
	160–200	77.18	78.0	Loss of MeSn +2,2′-bipyridine
	200–400	9.7	9.2	Loss of HCl
	400–485	9.7	9.3	Loss of HCl
	Over 450	3.7	3. 5	Residue: C
SC 2	27–125	–	–	Thermally stable
	125–400	96.81	97.01	Loss of MeSn +4,4′-bip + 2HCl + H_2
	Over 400	3.19	2.99	Residue: C
SC 3	27–200	–	–	Thermally stable
	200–340	62.09	62.55	Loss of MeSnCl + pyridine
	340–400	9.89	9.99	Loss of 0.5 pyridine
	400–450	11.22	11.95	Loss of HCl +0.5 NH_3
	Over 500	15.02	15.51	Residue: 5C

Table 10
Diameter of inhibition zones (mm) for the tested compounds against different species of microorganisms.

Compounds	Inhibition zone/mm			
	Staphylococcus aureus G$^+$-Bacteria	Bacillus cereus *G$^+$-Bacteria*	*Candida albicans Yeast*	*Aspergillus niger Fungus*
SC 1	15	–	9	18
SC 2	25	28	6	5.5
SC 3	30	15	9	11
Ampicillin *Antibacterial*	18	9	0	0
Amphotericin B *Antifungal*	0	0	19	17

be stable up to 125 °C. The degradation profile occurs in one step starting from 125 °C to 400 °C, This step corresponds to the loss of the more volatile connecting unit MeSn, 4,4′-bipyridine, two molecules of HCl and Hydrogen, Δm % obser. (calcd): 97.01 (96.81). The weight of the residue obtained after complete degradation is consistent with carbon Δm % obser. (calcd): 2.99 (3.19), Table 9. The degradation profile of **SC3** indicates that the framework of the organotin complex is stable up to 200 °C. The degradation process takes place in three steps, Fig. S15 and Table 9. The first step starts from 200 °C up to 340 °C. This step corresponds to the release of (MeSnCl) and pyridine moiety as a result to the decomposition of 1,10-phenanthroline ligand, Δm % obser. (calcd): 62.55 (62.09). The weight loss in the second step within temperature range 340–400 °C is due to the decomposition of 0.5 (pyridine moiety), Δm % obser. (calcd): 9.99 (9.89). The weight loss in the third step in the temperature range 400–450 °C corresponds to the loss of HCl and 0.5(NH_3), Δm % obser. (calcd): 11.95 (11.22). Over 450 °C, complete degradation occurs and the residue obtained is coincident with 5(carbon), Δm % obser. (calcd): 15.51 (15.02).

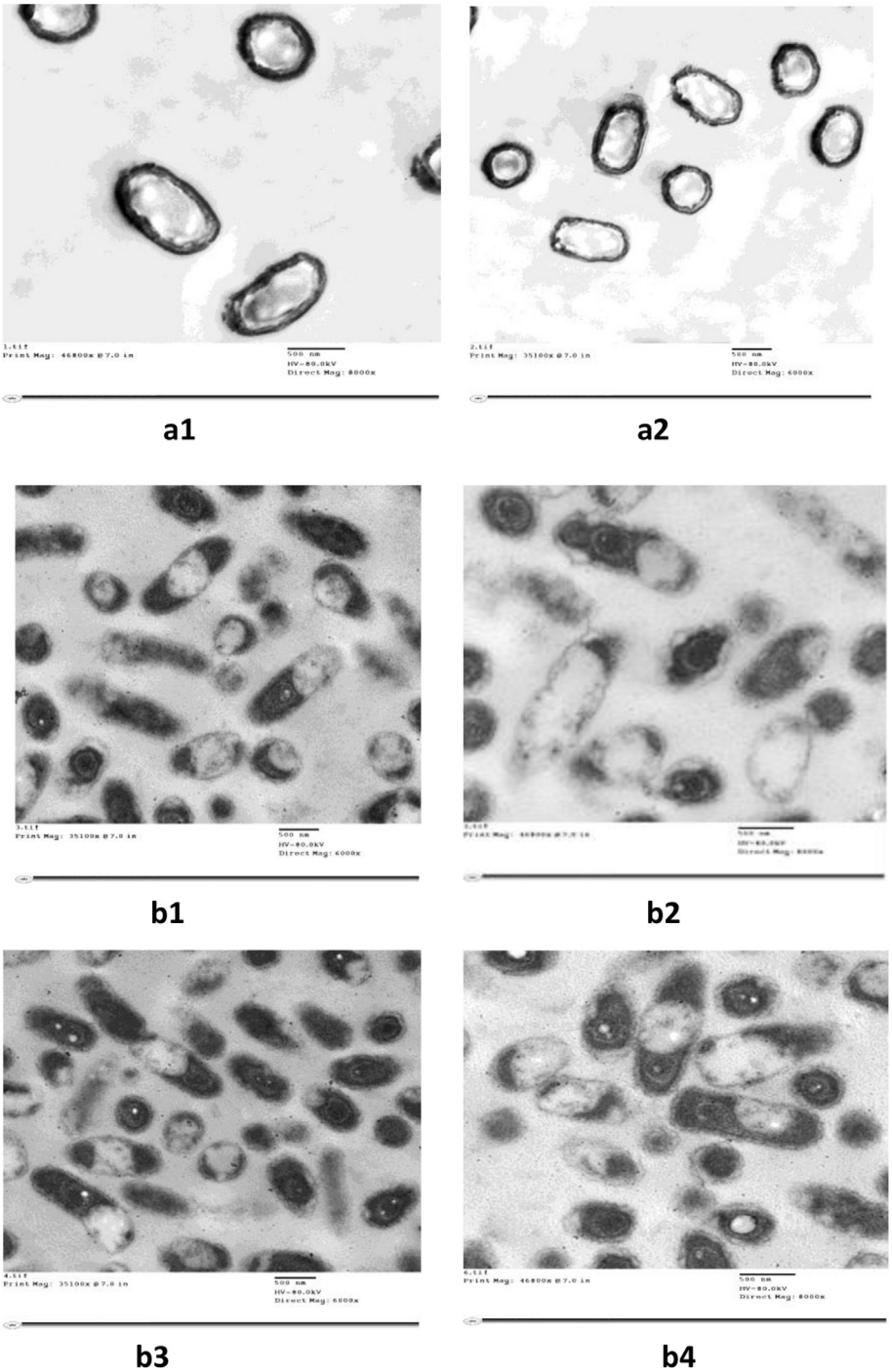

Fig. 13. Transmission electron microscopic images of Bacillus cereus cells; (a1) grown in the control, (a2) structure of bacterial cells in the media containing 10 μg/mL of SC 2 and (b1-b4) cytoplasmic vacuolation in the bacterial cell, distortion and disruption of bacterial cell wall.

Table 11
Antioxidant and anti-hemolytic activities compared with ascorbic-acid.

Compounds	Antioxidant activities	Anti-hemolytic activities
	ABTS Inhibition % = Abs(blank) -Abs(sample)/Abs(blank) X 100	*Erythrocyte hemolysis % = Abs(sample)/Abs(blank) X 100*
Ascorbic-acid	89.1%	4.4%
SC 1	49.6%	7.0%
SC 2	25.7%	84.9%
SC 3	32.3%	89.3%

4. Antimicrobial assessment

The antimicrobial activity of the three supramolecular complexes were evaluated against one of gram positive bacteria (*Staphylococcus aureus and* Bacillus cereus*)*, a specie of fungi *(Aspergillus niger)* and a specie of yeast-like fungi (*Candida albicans)*, Table 10. The results detected that SC **2** and SC **3** exhibit very strong inhibitory effects (inhibition zone diameters are 25 and 30 mm) on the growth of *Staphylococcus aureus* compared with that of Ampicillin (inhibition zone diameter is 18 mm), Fig. S 16.

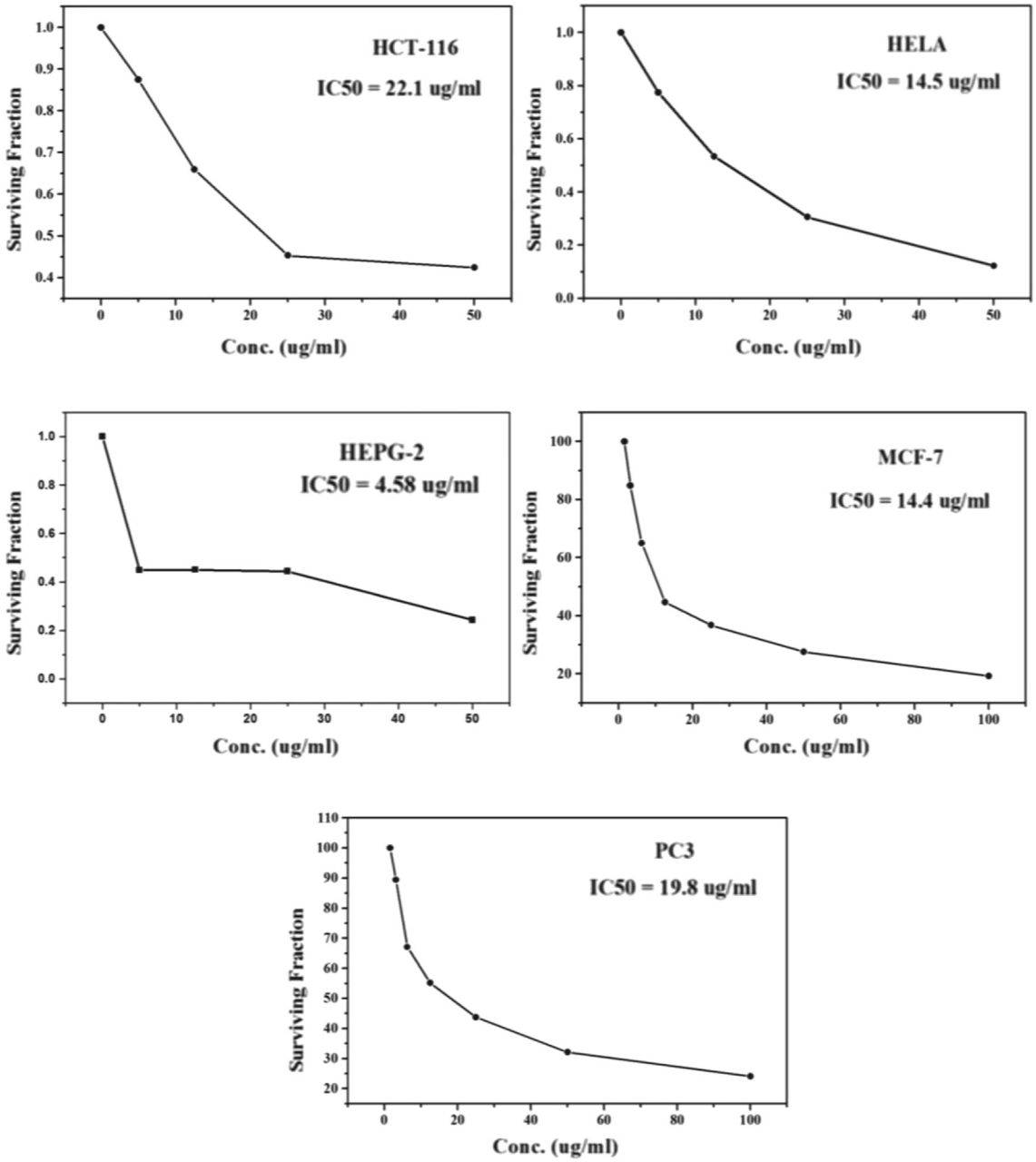

Fig. 14. Survival curves of SC 1 toward some tumor cell lines.

Whereas, SC **1** exhibits strong inhibitory effect (inhibition zone diameter is 15 mm) compared with that of Ampicillin (antibacterial drug) effect. SC **1** and SC **3** exhibit medium inhibitory effects (inhibition zone diameter is 9 mm) on the growth of ***Candida albicans*** compared with that of **Amphotericin B** (antifungal drug). However, **SC 2** shows weak inhibitory effect (inhibition zone diameter is 6 mm). Moreover, SC **1** displays very strong inhibitory effects (inhibition zone diameter is 18 mm) on the growth of *Aspergillus niger* compared with that of **Amphotericin B** (antifungal drug). Whilst, SC **2** and SC **3** display moderate and weak inhibitory effects (inhibition zone diameters are 11 and 5.50 mm, respectively) on the growth of *Aspergillus niger* compared with that of **Amphotericin B**. Table 10. These findings were confirmed by the determination of the minimum inhibitory concentration (MIC) of the tested compounds, Table S1. The higher antimicrobial activity can be proved by low MIC values. It was observed that the concentration of 12.5 mg/

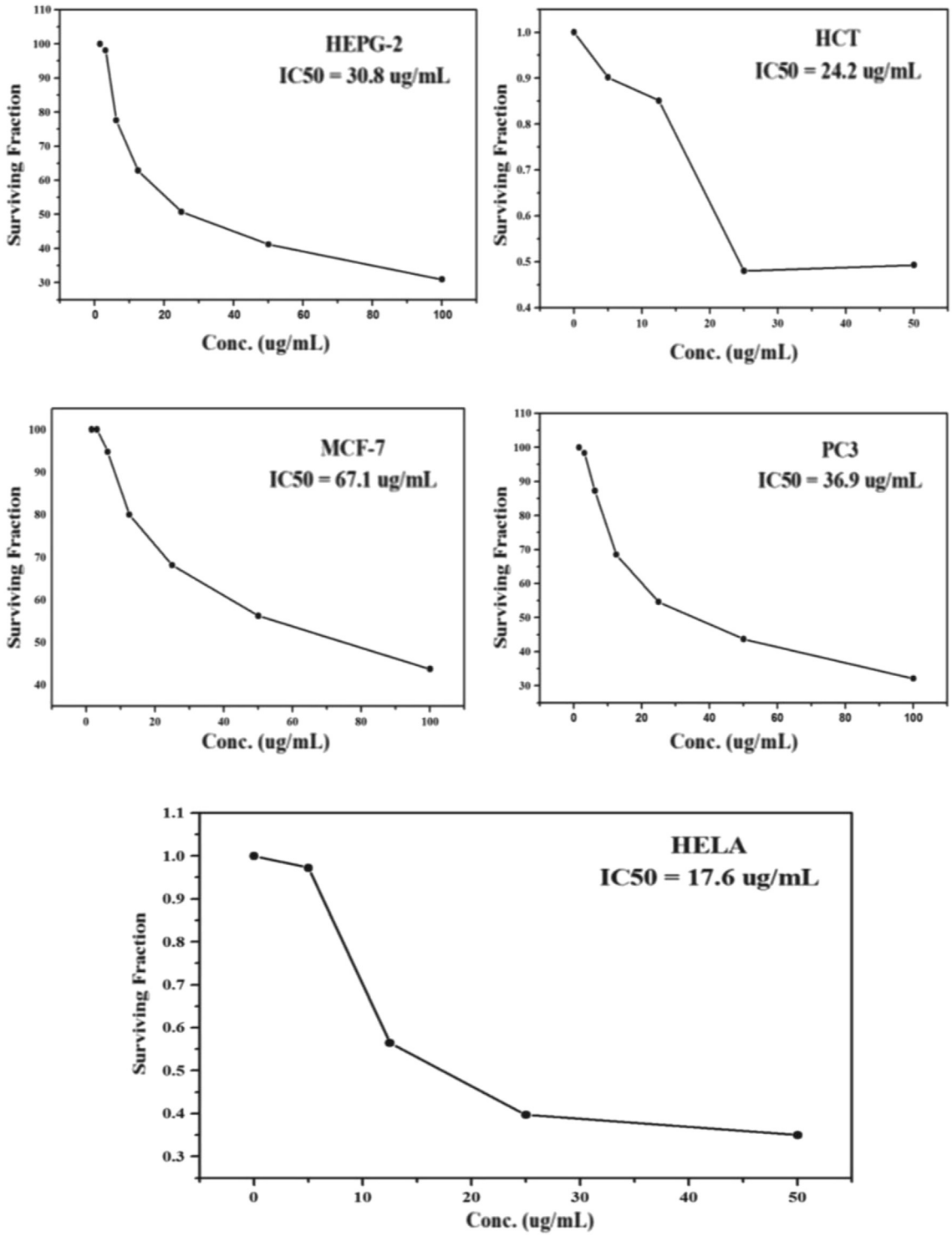

Fig. 15. Survival curves of SC 2 toward some tumor cell lines.

mL (SC **1**) was recorded as the lowest concentration and the most highly effective MIC value against Aspergillus niger and *Staphylococcus aureus*, Tables 11 and S2 and Fig. S17. Moreover, the antimicrobial activity of SC 2 exhibits the highest inhibition zone; 28 and 25 mm for *B. cereus* and *S. aurous*, respectively. The effect of SC 2 on *Bacillus cereus* cells growing in the nutrient broth media containing 10 μg/mL of SC **2** was studied by Transmission Electron Microscope (TEM), Fig. 13. TEM analysis of thin sections prepared from *Bacillus cereus* cells allows direct visualization of intracellular morphological changes of bacterial cells after treatment with SC **2**. Nutrient agar medium was prepared containing 10 μg/mL of SC **2** and the bacterial cells were then inoculated in the nutrient broth medium and incubated for 24 h. The bacterial cells (Control) were in normal sizes with intact intracellular structures and well-maintained contents. On the other hand, *Bacillus cereus* cells growing in the nutrient broth media containing 10 μg/mL of SC **2** were clearly damaged. The membranes of the bacterial cells were deformed and intracellular structures were disorganized. Many null cells were found in the bacterial samples treated with SC **2**, indicating that the intracellular contents had leaked out of the cells owing to the damage and disorganization of the cell membrane, Fig. 13.

5. Anti-oxidant and anti-hemolytic activities

The antioxidant activity for the tested compound **1** was measured using 2, 2′- azino-bis (3-ethyl benzthiazoline-6-sulonic acid) (ABTS) method. The antioxidant activity assay employed here is one of the several assays that depend on measuring the consumption of stable free radicals, that is, evaluate the free radical-scavenging activity of the investigated component. The methodology assumes that the consumption of the stable free radical (X•) will be determined by the following reactions:

$$XH + Y^{\bullet} \rightarrow X^{\bullet} + YH$$

The rate and the extent of the process measured in terms of the decrease in $X^{\bullet}$ concentration would be related to the ability of the added tested compound to trap free radicals. The decrease in color intensity of the free radical solution due to scavenging of the free radical by the antioxidant material is measured calorimetrically at a specific wavelength. The assay employs the radical cation derived from (ABTS) to assess antioxidant potential of the investigated compound. The tested compound **SC 1** exhibits moderate antioxidant activity compared with ascorbic acid. However, **SC 2** and **SC 3** show weak activity. On the other hand, the ability to inhibit rate

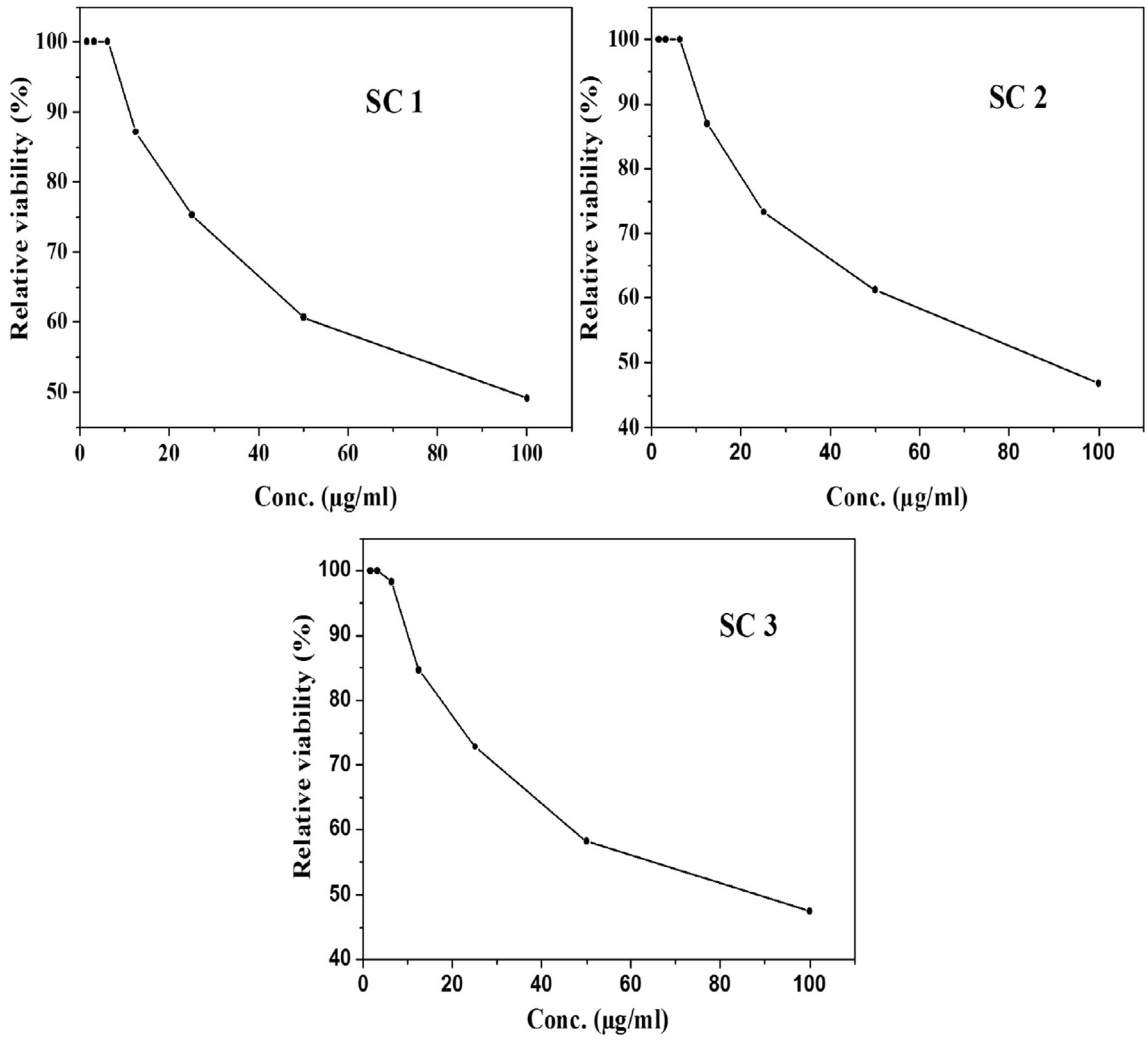

Fig. 16. Survival curves of SC 3 toward some tumor cell lines.

Table 12
Cytotoxic activity against some human tumor cells and normal WI-38 cells.

Compounds	In vitro Cytotoxicity IC50 (μg/ml)					
	HEPG-2	HCT-116	PC3	MCF-7	HELA	WI-38
5-Fluorouracil	7.9 ± 0.28	5.2 ± 0.14	8.3 ± 0.25	5.5 ± 0.21	5.1 ± 0.12	6.7 ± 0.51
SC 1	4.58 ± 1.15	22.1 ± 1.81	19.8 ± 1.44	14.4 ± 1.52	14.5 ± 1.11	85.2 ± 4.62
SC 2	30.8 ± 2.40	24.2 ± 3.47	36.9 ± 2.93	67.1 ± 4.35	17.6 ± 1.11	80.4 ± 4.38
SC 3	4.43 ± 0.43	40 ± 0.75	29.3 ± 1.87	24.4 ± 0.48	11.5 ± 0.96	78.2 ± 4.13

• IC50 (μg/ml): 1–10 (very strong), 11–20 (strong), 21–50 (moderate), 51–100 (weak) and above 100 (non-cytotoxic).

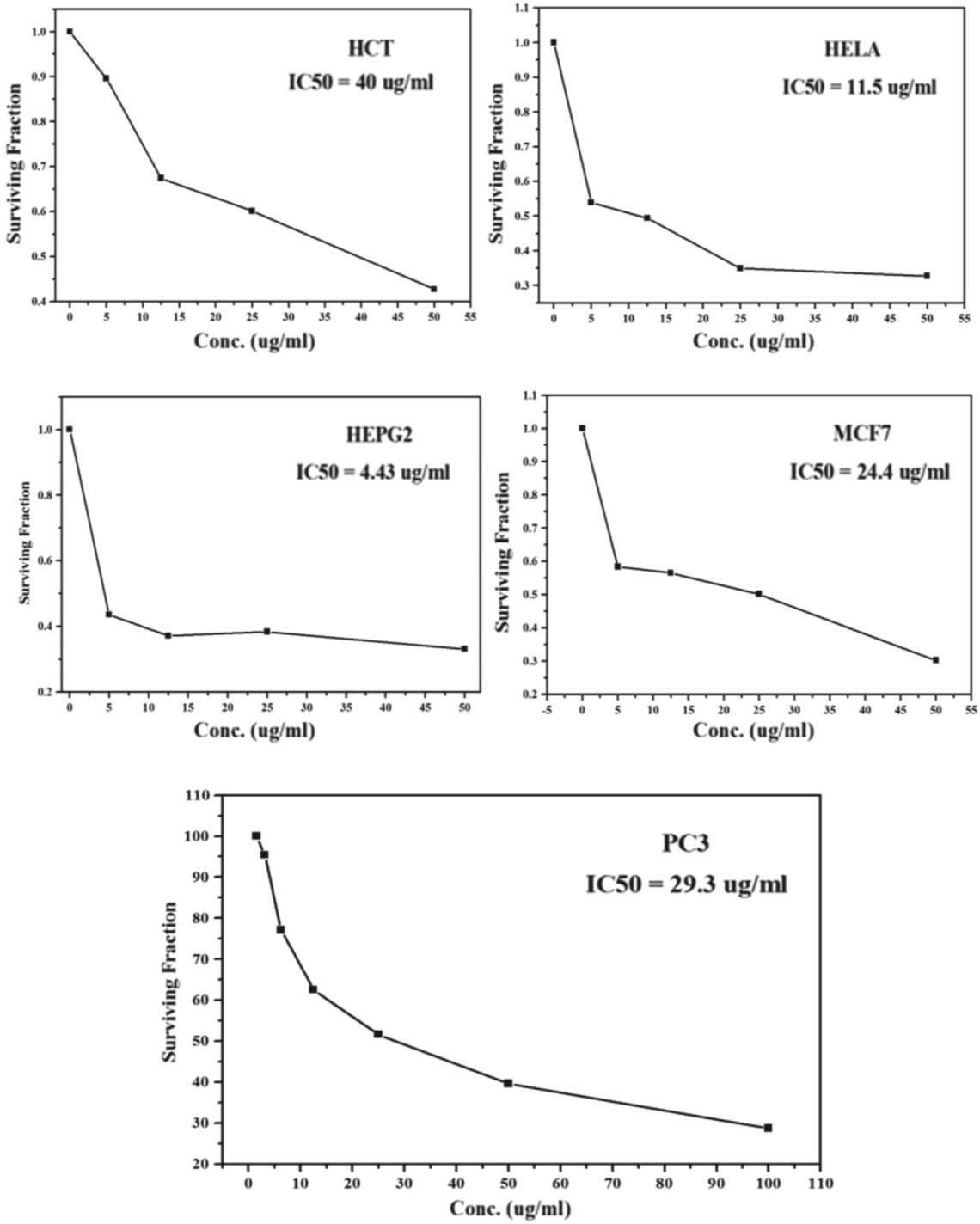

Fig. 17. Relative viability (%) of normal WI-38 cells at various concentrations of SC 1, SC 2 and SC 3.

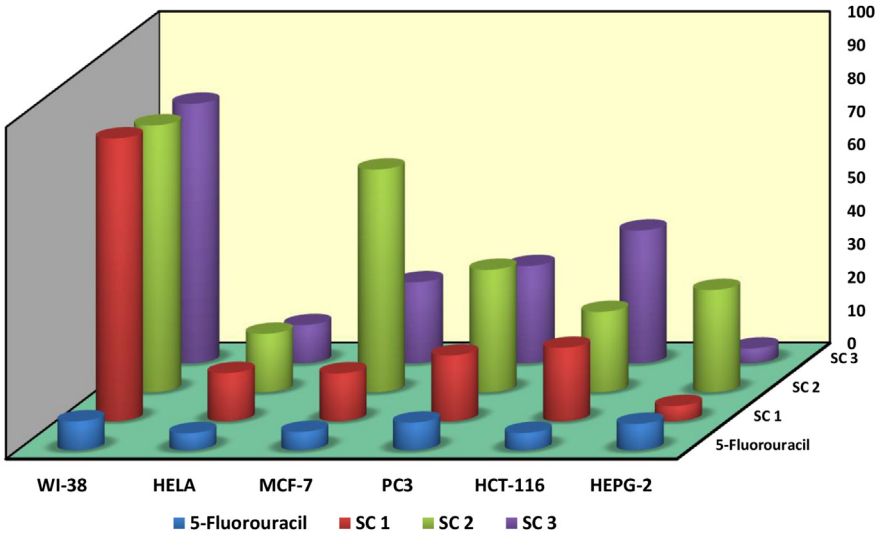

Fig. 18. In vitro cytotoxicity of SC 1–3 against non-tumorigenic Human lung fibro blast; WI-38 cell line and various human cancer cell lines, using IC50 values.

erythrocyte hemolysis was examined. The data revealed that **SC 1** exhibits the most potent anti-hemolytic activities compared with ascorbic-acid. However, **SC 2** and SC **3** show very weak or no anti-hemolytic activities, as shown in Table 11.

6. Cytotoxic activity

In vitro potential cytotoxicity of **SC 1**–**3** was tested against human breast adenocarcinoma cell line (MCF7), liver carcinoma (HEPG2), colorectal carcinoma (HCT-116), cervical carcinoma (HELA) and prostate cancer (PC3) cell lines, Fig. S 18, as well as against Human lung fibro blast cell line (WI-38) as a normal cell line for comparison. The relations between surviving fraction and drugs concentration are plotted to get the survival curve of each tumor cell line indicating that the tested compounds are able to inhibit the growth of the cancer cell lines under investigation in a dose-dependent manner, Figs. 14–16. These dose response curves were constructed in order to determine the effective dose, IC_{50}, which is the concentration of drug that reduces cell growth by 50% under the experimental conditions and is the average from at least three independent determinations, Table 12. The results of the cytotoxic assays showed that the tested compounds **SC** 1 and **SC 3** have very strong significant bioactivity towards human HEPG-2 cell line than 5-Fluorouracil. On the other hand, all tested compounds exhibit strong cytotoxic activity toward HELA cell line and moderate cytotoxic activity toward HCT-116 cell line. However, **SC 1**–**3** exhibit moderate cytotoxic activity toward PC 3. It is worth noting that **SC 1** revealed strong cytotoxic activity toward the five cell lines. However, **SC 2** exhibits the weakest cytotoxic activity toward MCF-7. To examine if our active compounds **SC 1**–**3** have a cytotoxic effect, they were tested against non-tumorigenic WI-8 cell lines. **SC 1**–**3** showed $IC_{50} = 85.2$, 80.4 and 78.2 μ M, respectively, against WI-38, Figs. 17 and 18 and Tables 12 and 13. These results indicate that the tested compounds do not exhibit cytotoxic effects on normal, non-tumorigenic WI-38 cell lines compared to the investigated cancer cells. The cytotoxic activity behavior of **SC 1**–**3** towards the tested cell lines are in accordance with the results of the prototype compounds reported in the literature [15]. The inhibition effects of **SC 1** and **3** are higher than that of **SC 2** or other organotin complexes, presumably due to the higher lipophilicity of the former complexes than **SC 2** leading to better cytostatic activity [15]. These results

Table 13
Relative viability of normal WI-38 cells (%).

Concentrations (μg/ml)	Relative viability of WI-38 cells (%)			
	5-FU	SC 1	SC 2	SC 3
100	7.5	49.1	46.8	47.5
50	14.2	60.7	61.2	58.2
25	21.4	75.3	73.3	72.8
12.5	33.1	87.2	86.9	84.6
6.25	50.6	100	100	98.3
3.125	65.0	100	100	100
1.56	87.3	100	100	100

encourage further investigation in vitro and in vivo of **SC 1**–**3**. Generally, in the present study, the tested compounds **SC 1**–**3** were found to inhibit cell proliferation and induce high % of apoptotic cancer cells in vitro model. Taken together, the active compounds exhibited significant and selective decreases in cell viability of HEPG-2, HELA and MCF-7 cancer cell lines and induced apoptosis within short times of treatment.

7. Conclusion

The structures of **SC 1**–**3** extend to create 2D- or 3D-dimensional networks through extensive hydrogen bonds and π–π stacking. The Sn atoms acquire octahedral geometry. The **SC 1**–**3** exhibited a decrease in cell viability against various human cancer cell lines with good selectivity as indicated by their lower toxicity against normal cells. Also, they were screened for their antioxidant, anti-haemolytic, antibacterial and antifungal activities. The tested compounds revealed better activity against Gram-positive than Gram-negative bacteria. The **SC 1**–**3** compounds need further investigations to advance to pre-clinical development and determine the exact mechanism of drug action. **1**–**3** are luminescent materials that can be used in applications as molecular sensing systems.

Acknowledgements

The authors are grateful to Tanta University, Tanta, Egypt that supports this work. This is gratefully acknowledged.

Appendix A. Supplementary data

Supplementary data to this article can be found online at https://doi.org/10.1016/j.jorganchem.2019.05.007.

References

[1] (a) J.-M. Lehn, in: Supramolecular Chemistry: Concepts and Perspectives, Vch, Weinheim, 1995;
(b) J.L. Atwood, G.W. Gokel, L. Barbour, in: Comprehensive Supramolecular Chemistry II, Elsevier, 2017.
[2] J.-M. Lehn, Chem. Eur J. 5 (1999) 2455–2463.
[3] A. Jana, S. Mandal, K. Singh, P. Das, N. Das, Inorg. Chem. 58 (3) (2019) 2042–2053.
[4] M. Sirajuddin, S. Ali, V. McKee, A. Wadood, M. Ghufrand, J. Mol. Struct. 1181 (2019) 93–108.
[5] Q. Li, F. Wang, R.-F. Zhang, J. Cui, C. Ma, Polyhedron 85 (2015) 361–368.
[6] T. Zöller, K. Jurkschat, Inorg. Chem. 52 (2013) 1872–1882.
[7] S. Shujah, R. Ziaur, N. Muhammad, A. Shah, S. Ali, A. Meetsma, Z. Hussain, J. Organomet. Chem. 759 (2014) 19–26.
[8] (a) A.V. Ţopîrlan, A.A. Patrascu, A. Sava, Delia-Laura Popescu, C. Silvestru, I. Haiduc, M. Andruh, J. Organomet. Chem. 882 (2019) 58–63;
(b) T.S. Basu Baul, A. Paul, L. Pellerito, M. Scopelliti, A. Duthie, D. de Vos, R.P. Verma, U. Englert, J. Inorg. Biochem. 107 (2012) 119–128.
[9] (a) R. García-Zarracino, H. HÖpfl, Angew. Chem. 116 (2004) 1533–1537. Angew. Chem., Int. Ed. Engl. 43, (2004) 1507-1511;
(b) R. García-Zarracino, H. HÖpfl, J. Am. Chem. Soc. 127 (2005) 3120–3130;
(c) R. García-Zarracino, J. Ramos-Quiñones, H. HÖpfl, Inorg. Chem. 42 (2003) 3835–3845.
[10] (a) J. Beckmann, D. Dakternieks, A. Duthie, F.S. Kuan, K. Jurkschat, M. Schürmann, E.R.T. Tiekink, New J. Chem. 28 (2004) 1268–1276;
(b) M. Mehring, G. Gabriele, S. Hadjikakou, M. schürmann, D. Dakternieks, K. Jurkschat, Chem. Commun. 8 (2002) 834–835;
(c) M. Mehring, I. Paulus, B. Zobel, M. Schürmann, K. Jurkschat, A. Duthie, D. Dakternieks, Eur. J. Inorg. Chem. 1 (2001) 153–160, 2001.
[11] M. Gielen, Tin Chemistry: Fundamentals, Frontiers and Applications, John Wiley & Sons Ltd, 2008, pp. 201–230.
[12] (a) L. Pellerito, L. Nagy, Coord. Chem. Rev. 224 (2002) 111–150;
(b) A. Chaudhary, M. Agarwal, R.V. Singh, Appl. Organomet. Chem. 20 (2006) 295–303;
(c) A. Chaudhary, R.V. Singh, Main Group Met. Chem. 31 (2008) 107–156.
[13] (a) M. Gielen, Coord. Chem. Rev. 151 (1996) 41–51;
(b) M. Gielen, E.R.T. Tiekink (Eds.), Metallotherapeutic Drug and Metal-Based Diagnostic Agents: ^{50}Sn Tin Complexes and Their Therapeutic Potential, 2005, pp. 421–435;
(c) M. Gielen, Appl. Organomet. Chem. 16 (2002) 481–494.
[14] (a) A. Penninks, M. Bol-Schoenmakers, W. Seinen, in: M. Gielen (Ed.), Nato ASI Series, Springer, Berlin, 1990, pp. 169–190;
(b) C. Pettinari, F. Marchetti, A. Cingolani, A. Lonrenzotti, E. Mundorff, M. Rossi, F. Caruso, Inorg. Chim. Acta 262 (1997) 33–46;
(c) C.E. Carraher Jr., M.R. Roner, J. Organomet. Chem. 751 (2014) 67–82.
[15] S. Wang, Q.-L. Li, R.-F. Zhang, J.-Y. Du, Y.-X. Li, C.-L. Ma, Polyhedron 158 (2019) 15–24.
[16] M.-L. Tong, J.-W. Cai, X.-L. Yu, X.-M. Chen, S.W. Ng, T.C. Mak, Aust. J. Chem. 51 (1998) 637–641 (Wrong Ref).
[17] S.M. Woessner, J.B. Helms, Y. Shen, B.P. Sullivan, Inorg. Chem. 37 (1998) 5406–5407.
[18] M.M. Rodriguez-Ramos, J.J. Wilker, J. Biol. Inorg. Chem. 15 (2010) 629–639.
[19] D.N. Sredojević, P.V. Petrović, G.V. Janjić, E.N. Brothers, M.B. Hall, S.D. Zarić, J. Mol. Model. 22 (2016) 30.
[20] S.A. Sadeek, S.M. Abd El-Hamid, W.H. El-Shwiniy, Res. Chem. Intermed. 42 (2016) 3183–3208.
[21] G. Singh, C.P. Singh, R. Frohlich, J. Therm. Anal. Calorim. 85 (2) (2006) 425–431.
[22] J. Soleimannejad, H. Aghabozorg, S. Hooshmand, M. Ghanbari, F. Manteghi, M. Shamsipur, J. Iran. Chem. Soc. 7 (2) (2010) 405–418.
[23] A.C. Kathalikkattil, P.S. Subramanian, E. Suresh, Inorg. Chim. Acta 365 (2011) 363–370.
[24] Z.R. Ranjbar, A. Morsali, Polyhedron 30 (2011) 929–934.
[25] S. El-din H. Etaiw, A.S. Badr El-din, J. Inorg. Organomet. Polym. 22 (2012) 478–491.
[26] S. El-din H. Etaiw, S.N. Abdou, A.S. Badr El-din, J. Inorg. Organomet. Polym. 25 (2015) 1478–1485.
[27] S.A. Bajur, F.B. Bramwell, M. Charles, F. Cervantes-Lee, K. Pannell, Inorg. Chim. Acta 197 (1992) 83–87.
[28] S.W. NG, Acta Crystallogr. C54 (1998) 1393–1395.
[29] G.M. Sheldrick, SHELXS-97, Program for Solution of Crystal Structures, University of Göttingen, Germany, 1997.
[30] T.G. Pridham, L.A. Lindenfelser, O.L. Shotwell, F.H. Stodola, R.G. Benedic, C. Foley, R.W. Jackson, W.J. Zaumeyer, W.H. Preston, J.W. Mitchell, Antibiotics against plant disease. I. Laboratory and greenhouse survey, Phytopathology 46 (1956) 568–575, 1956.
[31] A.B.A. El-Gazzar, A.M.S. Youssef, M.M. Youssef, A.A. Abu-Hashem, F.A. Badria, Eur. J. Med. Chem. 44 (2009) 609–624.
[32] E.A. Lissi, B. Modak, R. Torres, J. Escobar, A. Urza, Free Radic. Res. 30 (6) (1999) 471–477.
[33] A.B.A. El-Gazzar, H.N. Hafez, A.A. Abu-Hashem, A.S. Aly Phosphorus, Sulfur silicon relat, Elements 184 (2009) 379–405.
[34] R. Aeschlach, J. Loliger, B.C. Scott, A. Murcia, J. Butler, B. Halliwell, O.I. Aruoma, Food Chem. Toxicol. 32 (1994) 31–36.
[35] Y. Morimoto, K. Tanaka, Y. Iwakiri, S. Tokuhiro, S. Fukushima, Y. Takeuchi, Biol. Pharm. Bull. 18 (1995) 1417–1422.
[36] F. Denizot, R. Lang, J. Immunol. Methods 89 (2) (1986) 271–277.
[37] H.J. Mauceri, N.N. Hanna, M.A. Beckett, D.H. Gorski, M.J. Staba, K.A. Stellato, K. Bigelow, R. Heimann, S. Gately, M. Dhanabal, G.A. Soff, V.P. Sukhatme, D.W. Kufe, R.R. Weichselbaum, Nature 394 (1998) 287–291.
[38] E. Najafi, M.M. Amini, M. Janghouri, E. Mohajerani, S. Weng Ng, Inorg. Chim. Acta 415 (2014) 52–60.
[39] (a) B. Delley, J. Chem. Phys. 92 (1990) 508–517;
(b) B. Delley, Int. J. Quantum Chem. 69 (1998) 423–433;
(c) B. Delley, J. Chem. Phys. 113 (2000) 7756–7764;
(d) X. Wu ana, A.K. Ray, Phys. Rev. B 65 (2002), 085403;
(e) A. Kessi, B. Delley, Int. J. Quantum Chem. 68 (1998) 135–144.
[40] W.J. Hehre, L. Radom, P.V.R. Schleyer, J.A. Pople, Ab Initio Molecular Orbital Theory, John Wiley, New York, 1986.
[41] B. Hammer, L.B. Hansen, J.K. Nørskov, Phys. Rev. **B** 59 (1999) 7413–7421.
[42] A. Matveev, M. Staufer, M. Mayer, N. Rösch, Int. J. Quantum Chem. 75 (1999) 863–873.
[43] S. Sagdinc, B. Koksoy, F. Kandemirli, S.H. Bayari, J. Mol. Struct. 917 (2009) 63–70.
[44] H.H. Jaffé, M. Orchin, Theory and Applications of Ultraviolet Spectroscopy, John Wiley and Sons, Inc., 5th Printing, 1970.
[45] B. Valeur, Molecular Fluorescence Principles and Applications, Wiley-VCH Verlag GmbH, 69469 Weinheim, Federal Republic of Germany, 2002, p. 59.
[46] G.M. Badger, I.S. Walker, J. Chem. Soc. (1956) 122–126.